Physics – Uspekhi **69** (5) 420 – 441 (2026)

CONFERENCES AND SYMPOSIA

PACS numbers: 61.50.Ks, 62.20.F –, 64.60.Cn, 64.70.K –

Phase transformations at grain boundaries and with their participation *

B.B. Straumal, O.A. Kogtenkova, A.S. Gornakova

DOI: https://doi.org/10.3367/UFNe.2025.04.040018

Contents

Abstract. The phase transformations can take place not only in the bulk of solids but also in grain boundaries (intercrystalline boundaries). Firstly, these are the faceting–roughening phase transitions. They can be of either the first or the second order (continuous). The grain boundary (GB) facets are parallel to the densely packed planes of the coincidence sites lattices (CSL). CSL is the superlattice containing the matching crystal nodes of both grains. As the temperature decreases, the new facets with increasing CSL indices become equilibrium. When the temperature rises, the GB may become rough and completely lose its facets. Secondly, these are phase transitions from incomplete wetting of the GB with a melt or a second solid phase to complete one and vice versa. GB wetting phase transitions can also be of first or second order (continuous). In this case, the wetting phase is a 'true' bulk phase of arbitrarily high thickness. And finally, thirdly, thin layers of the intergarnular phase can form in GB when the lattices of two neighboring grains still interact with each other through it. This phase (for example, quasi-liquid one) is stable in GB, but unstable in the bulk. It can appear as a result of pre-wetting, pre-melting, or pseudo-incomplete wetting phase transformations. GB phase transformations affect the properties of the polycrystal as a whole and lead to the appearance of new GB lines in bulk phase diagrams.

B.B. Straumal [a], **O.A. Kogtenkova** [b], **A.S. Gornakova** [c]
Institute of Solid State Physics, Russian Academy of Sciences,
ul. Akademika Osipyana 2, 142432 Chernogolovka,
Moscow region, Russian Federation
E-mail: [a] straumal@issp.ac.ru, [b] kogtenkova@issp.ac.ru,
[c] alenahas@issp.ac.ru

Received 19 August 2025
Uspekhi Fizicheskikh Nauk **196** (5) 450 – 472 (2026)
Translated by the authors

Keywords: grain boundaries, phase transformations, faceting, roughening, wetting, pre-wetting, pre-melting, pseudo-incomplete wetting, complexions, phase diagrams, segregation, adsorption, mass transfer

1. Introduction

The grain boundary (GB) is the interface between two misoriented crystallites of the same composition. If the misorientation angle between two grains is less than approximately $\sim 15°$, then the boundary is classified as a small-angle grain boundary. In this scenario, it can be described as a wall of lattice dislocations that separate the regions where the lattice of one grain changes smoothly into the lattice of the other grain. Therefore, the small-angle grain boundary essentially consists of one-dimensional defects. When the misorientation angle exceeds about $\sim 15°$, the grain boundary becomes a two-dimensional defect with a thickness on the scale of the interatomic distance. These are different types of boundaries that will be discussed in this review.

Different phase transformations can take place in grain boundaries, similar to those within the bulk material. When examining the bulk phase transitions, the focus is on the free energy per unit volume. However, when dealing with internal interfaces like grain boundaries, the excess free energy per unit area of the interface plays a comparable role [1–4].

In this review, we will commence the discussion on GB phase transitions by examining faceting–roughening transitions (Section 2). These transformations can also occur in polycrystals made of pure components containing identical

* This review is based on the report presented for the Scientific Session of the Physical Sciences Division of the Russian Academy of Sciences (PSD RAS), on April 23, 2025 (see *Physics–Uspekhi* **69** (5) 419 (2026); *Uspekhi Fizicheskikh Nauk* **196** (5) 449 (2025)).

atoms. When the external faces are aligned parallel to the closely packed planes of the crystal lattice, the faces (facets) at the grain boundaries will be parallel to the closely packed planes of the superlattice formed by coinciding nodes shared by the two grains (so-called coincidence site lattice or CSL). At elevated temperatures, the low-index CSL facets are observable. As the temperature decreases, equilibrium facets emerge with higher indices. Subsequently, we will delve into the GB wetting phase transitions (Section 3). Within grain boundaries, the liquid phase or melt can manifest as continuous layers dividing adjacent crystallites (in cases of complete wetting) or chains of lenticular particles with a nonzero contact angle (in cases of incomplete wetting). The second phase that 'wets' the grain boundary could be not only liquid but also solid.

If the second phase completely wets the boundary in the two-phase region of the phase diagram, then upon replacing the grain boundary with the second phase interlayer, the system experiences an energy gain. This energy gain can stabilize a thin layer of the second phase in a GB even in the single-phase region where the second phase is unstable in the bulk (Section 4). Consequently, additional lines related to grain boundaries appear in the phase diagrams. These include wetting tie-lines in the two-phase regions of the phase diagram and extensions of these tie-lines into a single-phase region, which can be referred to as grain-boundary solidus or solvus. Thin layers of the grain boundary phase may also develop at the boundaries in cases of pseudo-incomplete wetting. The GB faceting–roughening transitions as well as GB wetting transformations can be of the first or of the second order (continuous). Grain boundary phase transitions can significantly impact various properties of polycrystals.

2. Grain boundary faceting–roughening

2.1 Faceting–roughening of free surfaces

The thermodynamics of external surfaces and internal interfaces, particularly the concept of excess free energy per unit surface area, was pioneered by Gibbs [1, 2]. He defined the free energy of the surface σ for a single-component material as the work $\mathrm{d}W$ required to create a new section of the surface $\mathrm{d}A$ at a constant temperature and chemical potential, given by $\sigma = \mathrm{d}W/\mathrm{d}A$. In the case of crystalline materials, this work is influenced by the atomic structure of the surface, meaning that for solid crystals, the value of σ also relies on the orientation of the surface or interface. Therefore, the free energy of a surface plays a crucial role in determining the conditions for the existence of two-dimensional phases on free and internal surfaces, as well as the phase transitions between these 2D phases [3, 4]. Among these transformations, phase transformations such as faceting–roughening stand out as particularly intriguing.

Historically, these phase transformations were among the earliest challenges in surface thermodynamics. The primary quest in free surface energy was to ascertain the crystal shape that would yield minimal total free energy, assuming a constant crystal volume. This mathematical challenge, independently formulated by Gibbs [1, 2] and Curie [5] as an orientation-dependent free energy surface integral, aimed to unravel the factors leading to the equilibrium faceting of crystal free surfaces during growth or dissolution. G.V. Wulff, a professor at Warsaw and later Kazan Universities in the late 19th century [6, 7], was the first to analyze the solution to this problem. Decades later, in the 1950s, L.D. Landau discussed the significance of step formation on flat crystal faces for equilibrium cutting [8]. Researchers like Barton, Cabrera, Chernov demonstrated that at a nonzero temperature, step formation on a flat surface raises configuration entropy and lowers surface free energy [9–11]. With increased temperature, the equilibrium step concentration rises until it reaches an infinite value at a specific temperature, leading to the loss of stability of flat faces (a faceting–roughening phase transition). Numerous theoretical and experimental studies have scrutinized these phase transitions in detail [12–15]. For instance, research has shown how NaCl crystals alter shape as temperature rises, changing from their customary cubic form to rounded flat faces [16]. Additionally, experiments involving the deposition of thin gold or lead films on amorphous carbon substrates demonstrated the formation of solidified small droplets with specific equilibrium shapes due to temperature treatment, highlighting faceting–roughening transitions [17, 18]. Theoretical calculations employing the solid-on-solid model revealed that the denser the atomic packing on certain crystal planes, the greater the energy needed to form a step on these planes, ultimately affecting the temperature at which facets disappear (become rough) [19]. Consequently, as temperature decreases, the equilibrium crystal shape is expected to become more intricate with the emergence of new facets. However, this phenomenon is challenging to observe on metal free surfaces due to reduced atom mobility just below melting point, except for solid helium surfaces where atom mobility is unique due to quantum supermobility [20].

Grain boundaries can exhibit faceting as well. Faceting is a distinct trait of special (or coincidence) GBs. This phenomenon arises when two crystals forming the grain boundary share certain misorientations, causing nodes of one lattice to coincide with nodes of the other lattice, creating a common superlattice known as a coincident sites lattice (CSL). These particular misorientations are referred to as coincident misorientations. The most prominent grain boundary facets tend to occur in densely packed CSL planes [21, 22]. In this scenario, densely packed CSL planes play a role akin to densely packed lattice planes in shaping the facet of a crystal's free surface. The intriguing phase transitions linked to the appearance and disappearance of crystal facets on outer surfaces, and how the orientation of these surfaces influences faceting phase transitions, are likely mirrored at grain boundaries [23–25]. For instance, studies by Smith and Balluffy [26, 27] have shown that facets at grain boundaries in aluminum and gold diminish as temperature rises towards the melting point, suggesting the occurrence of a roughening phase transition at grain boundaries as well. The behavior of tilt boundaries in copper near a $\Sigma 5$ coincidence misorientation has also been elucidated through the concept of faceting–roughening GB phase transition [28].

2.2 Faceting–roughening of twin ($\Sigma = 3$) grain boundaries in copper

In metals with a face-centered cubic (fcc) lattice featuring low or moderate stacking-fault energy, twin grain boundaries $\Sigma 3$ and related grain boundaries $\Sigma 3^2$ ($\Sigma 9$) and $\Sigma 3^3$ ($\Sigma 27$) are prevalent [29–31]. For instance, in an annealed fcc polycrystal, coherent twins typically account for 10–50% of the total GB area [32]. This can be attributed to the remarkably low energy levels of coherent twins in fcc metals. In nickel, for instance, the energy of a coherent twin is merely 0.064 J m^{-2},

equivalent to just 0.058 of the average GB energy in nickel [33]. In contrast, the energy of coherent twins in bcc metals is relatively higher. In the case of bcc iron, the energy of a coherent twin is 0.26 J m^{-2}, which corresponds to 0.23 of the average GB energy in a Fe polycrystal [29]. Consequently, in ferritic steels, the portion of coherent twins among all GBs is only around 3% or even lower [34, 35]. However, within special grain boundaries, such as in bcc metals, coherent twins prevail [29]. Twins also hold a distinctive significance in metals with a hexagonal lattice [36] and in semiconductor materials [37]. Therefore, we will examine the various details of faceting–roughening phenomena through the lens of twin ($\Sigma = 3$) grain boundaries.

From a standpoint of facet formation, the coincidence sites lattice (CSL) serves a comparable role in grain boundaries to than of the crystal lattice within the bulk material for the development of faces on external surfaces. As temperature decreases, the facets of external surfaces stabilize with progressively lower atomic packing densities. Likewise, as temperature drops, an increasing number of facets with reduced densities of coincidence sites are expected to emerge on the GBs [38]. Just as at low temperatures, distinct properties manifest in GBs with diminished densities of coincidence sites (and larger coincidence parameter Σ) [39]. This phenomenon was indeed witnessed in [40]. A study in this context delved into grain boundary faceting for $\Sigma = 3$ CSL within the temperature range of 0.5 to 0.95 T_m (where $T_m = 1356$ K is the copper melting point). Cylindrical bicrystals containing two concentric grains were grown from the melt for this investigation, resulting in a tubular-shaped GB [40]. When dealing with a closed cylindrical boundary within a bicrystal, the capillary driving force during annealing prompts the boundary to move towards the sample axis, thereby reducing its area. As per Wulff's work, slowly growing or dissolving crystals conform closely to equilibrium shapes [41, 42]. Typically, the energy disparity among facets of varying orientations is minimal and insufficient to ensure kinetic convergence to an equilibrium GB shape. Consequently, gradual GB migration driven by capillary forces facilitates the attainment of an equilibrium shape. A similar approach was utilized to examine grain boundary transformations from a special boundary to a general one for $\Sigma 17$ GB in tin [43].

In the bicrystal examined in Ref. [40], the outer and inner grains established a coincidence sites lattice where every third node coincide perfectly, denoted as $\Sigma = 3$. This $\Sigma = 3$ value represents the minimum possible parameter Σ for coincidence sites lattice between two fcc crystals. Throughout the entire temperature range under investigation, it was observed that the facets (or faces) of $\Sigma = 3$ GB intersect each other, forming completely flat faces with no discernible rounded corners between facets.

Figure 1 presents a series of micrographs displaying $\Sigma 3$ facets with different indices. They are parallel to different CSL planes. These facets intersect the $(100)_{CSL}$ facet. The $(100)_{CSL}$ facet boasts the highest density of coinciding sites, creating a symmetrical twin boundary. The micrographs were captured from samples annealed at varying temperatures and quenched in water. Each micrograph is accompanied by a cross-section of the coincidence site lattice $\Sigma 3$ on the left, indicating the facet positions. Above a temperature of $0.8T_m$, only two distinct grain boundary facets are observable in the samples, namely, the densely packed $(100)_{CSL}$ facet and the non-CSL 9R facet. The $(100)_{CSL}$ facet, also known as a symmetric twin boundary, is structured by the parallel, densely packed planes $\{111\}_1$ and $\{111\}_2$ of both fcc grains. Unlike gold twin plates [49], twin plates in copper do not

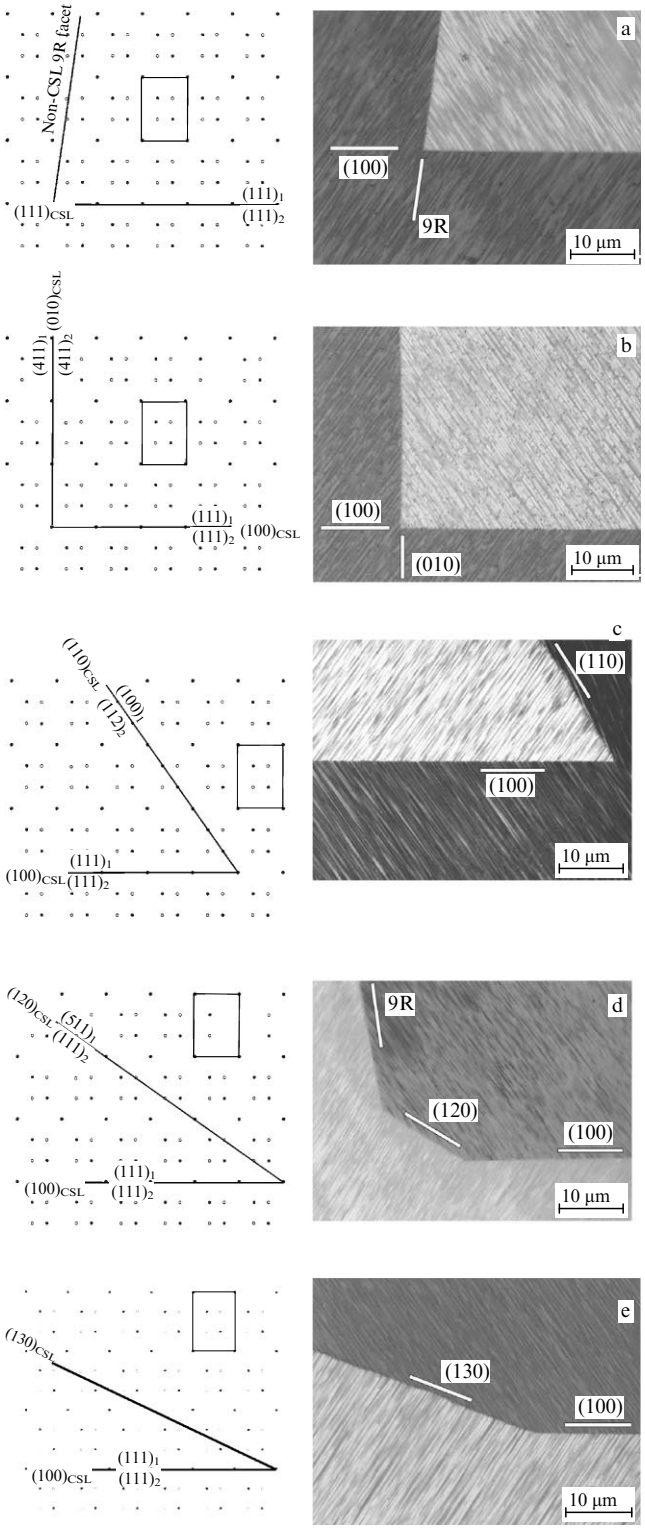

Figure 1. The sections of $\Sigma 3$ coincidence sites lattice, perpendicular to the rotation axis {110} of the lattices of both grains, showing the orientation of various GB facets (on the left side) and micrographs depicting the intersections of $(100)_{CSL}$ facet with other facets (on the right side) in bicrystals subjected to different annealing temperatures. (a) $(100)_{CSL}$ and 9R facets at 1293 K. (b) $(100)_{CSL}$ and $(010)_{CSL}$ facets at 673 K. (c) $(100)_{CSL}$ and $(110)_{CSL}$ facets at 923 K. (d) $(100)_{CSL}$ and $(120)_{CSL}$ facets at 973 K. (e) $(100)_{CSL}$ and $(130)_{CSL}$ facets at 673 K. This illustration has been reproduced from reference [40] with permission from Elsevier © 2006.

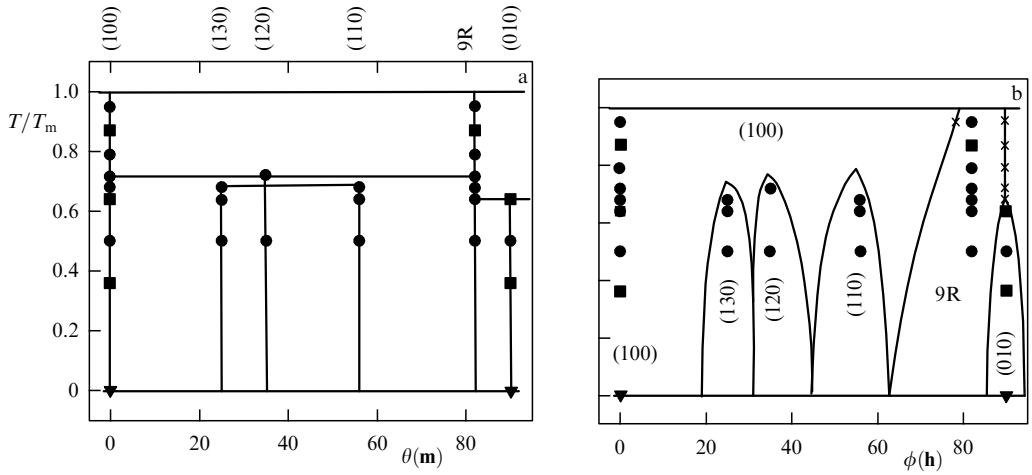

Figure 2. (a) Illustrates the (T, θ) and (b) (T, θ) phase diagrams for $\Sigma 3$ {110} tilt grain boundaries in copper. The angular variables θ and ϕ are expressed in degrees and represent the orientation of the interface (**m**) and the shape of the crystal (**h**) in the equatorial section perpendicular to the {110} axis. In diagram (a) (T, θ), the positions of minima on the Wulff diagram are shown for temperatures below $T < T_{Rf}$. On the other hand, diagram (b) (T, θ) indicates the angular regions for the faceted areas of the GB. The experimental data points represented by circles (●) and crosses (x) are from Ref. [40], squares (■) are experimental data from Refs [23, 24, 44–47], and triangles (▼) denote simulation results [48]. This diagram is reproduced from [40] with the permission of Elsevier © 2006.

exhibit a rectangular appearance at high temperatures. The facets at the edges of each twin plate form an angle of $\varphi = 82°$ with the $(100)_{CSL}$ plane (as shown in Fig. 1a). The orientation angle φ represents the angle between a given grain boundary plane and the lowest-energy boundary orientation at $\varphi = 0°$ (in this case, the symmetrical twin boundary). The facet with a $\varphi = 82°$ angle does not align with any low-index CSL plane. The minimum grain boundary energy $\sigma_{GB}(\varphi)$ at $\varphi = 82°$ is linked to the presence of a thin grain boundary layer with the 9R structure, forming a plate of the grain boundary phase with bcc structure in the fcc matrix [50–53]. Theoretical studies predicted also further non-CSL GB facets [54]. The interfaces of $(100)_{CSL}/82°$9R facets at the twin plate ends display sharp, nonrounded edges between them.

As temperature decreases, additional facets begin to emerge in the equilibrium shape of the $\Sigma 3$ grain boundary. However, the edges that formed at higher temperatures do not disappear. This phenomenon is depicted in Fig. 2 through grain boundary phase diagrams. The newly introduced faces include $(010)_{CSL}$, $(110)_{CSL}$, $(120)_{CSL}$ and $(130)_{CSL}$, all of which exhibit lower packing density in the coincidence site lattice (CSL) compared to the $(100)_{CSL}$ facet. For instance, at $T = 673\ K = 0.5T_m$, six crystallographically distinct faces coexist on the $\Sigma 3$ grain boundary. The ridges between these faces are well-defined and sharp, rather than being rounded. Therefore, the emergence of new facets occurs at the sharp ridges between existing facets, unlike what is observed for surface facets in materials like lead, gold, or helium [17, 55–57]. The critical temperature, denoted as T_{Rf}, at which a less densely packed facet appears in the equilibrium GB shape is lower than the actual temperature at which this facet either appears or disappears. This concept is illustrated in Fig. 3 for facets such as $(010)_{CSL}$, $(110)_{CSL}$, $(120)_{CSL}$ and $(130)_{CSL}$. At temperature T_R, a shallow minimum appears on the curve $\sigma(\mathbf{m})$ (e.g., for the $(hkl)_{CSL}$ facet), indicating its metastable state. Only with a further decrease in temperature does this minimum deepen sufficiently to compete with existing facets, transitioning the metastable facet to a stable state and manifesting itself at T_{Rf} in the equilibrium GB shape. At the T_{Rf} point, the plane perpendicular to the radius vector at the

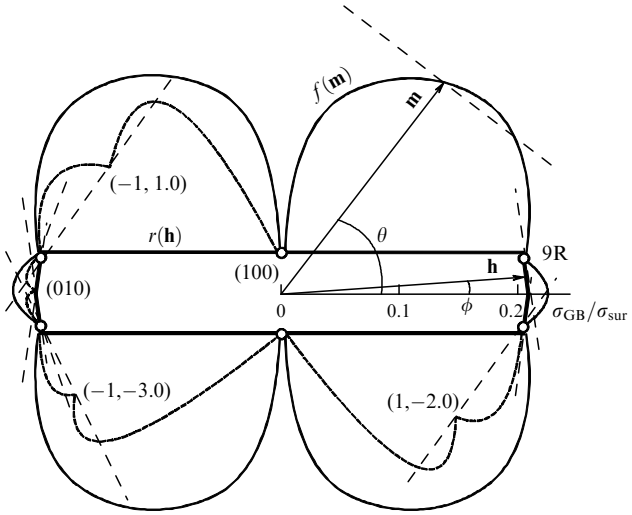

Figure 3. Wulff–Herring diagram representing the energy of the grain boundary $f(\mathbf{m})$ (depicted by a thin solid line) and the resulting equilibrium grain boundary shape (GB) $r(\mathbf{h})$ (displayed as a thick solid line) in a flat section perpendicular to the inclination axis {110} for the $\Sigma 3$ GB in copper at 1293 K. The open circles on the diagram indicate the GB energy σ_{GB} for the $(100)_{CSL}$ and 9R facets, determined from angle measurements at the top of the thermal etching groove using AFM. The angular variables θ and ϕ, expressed in degrees, describe the orientation of the interface (**m**) and the crystal shape (**h**), respectively. Additionally, the diagram includes the minima on $f(\mathbf{m})$ (shown as thin dotted curves) for the $(010)_{CSL}$, $(110)_{CSL}$, $(120)_{CSL}$ and $(130)_{CSL}$ facets with perpendicular planes touching $r(\mathbf{h})$. This representation is sourced from the study [40] with the permission of Elsevier © 2006.

corresponding intersection point on $\sigma(\mathbf{m})$ for the $(hkl)_{CSL}$ facet intersects with the curve $z(\mathbf{h})$, leading to the appearance of the $(hkl)_{CSL}$ facet in the equilibrium GB shape. By assuming constancy of at low temperatures, one can estimate values for less densely packed $(hkl)_{CSL}$ facets using the construction depicted in Fig. 3.

Based on the theory outlined in references [58, 59], the roughening transition follows the Berezinskii–Kosterlitz-Thouless mechanism [60–62] and is expected to occur at a

temperature T_R defined as:

$$kT_R = 2\gamma_R \frac{d^2}{\pi}, \quad (1)$$

here, k represents the Boltzmann constant, γ_R is the stiffness of the interface at T_R, and d denotes the interplane distance, which is the distance between the closest crystal planes measured perpendicular to the surface. Assuming isotropic interfacial tension [58, 59], the surface stiffness γ_R can be substituted with σ_{GB}. When dealing with a grain boundary, the determination of the distance d involves the coincidence site lattice [63] and the displacement shift lattice (DSC) [64], representing the height of the elementary step for each CSL facet. By using the stacking fault energy in copper (7.8×10^4 J m^{-2} [65] or 5.5×10^4 J m^{-2} [66]) for $\sigma_{(100)}$, we calculate T_R to be in the range of 1.4 to 1.9 times the melting point temperature T_m for the $(100)_{CSL}$ facet tin copper. By utilizing the given value $\sigma_{9R}/\sigma_{(100)} = 6$ (as shown in Fig. 3) in equation (1), we derive T_R to be between 0.9 and 1.3 times T_m for 9R facets. This observation signifies that the $(100)_{CSL}$ and 9R facets retain their faceted nature on the $\Sigma = 3$ grain boundary in copper up to the melting point T_m. Moreover, equation (1), developed to describe surface faceting loss based on the Berezinsky–Kosterlitz–Thouless theory [60–62], is also valid for grain boundary faceting. Therefore, by substituting the actual appearance temperature T_{Rf} of each face into equation (1) instead of T_R it becomes feasible to once again estimate the values of $\sigma_{hkl}/\sigma_{(100)}$ for less densely packed CSL facets $(hkl)_{CSL}$. Any discrepancies with the estimates of $\sigma_{hkl}/\sigma_{(100)}$ derived from the Wulff diagram may stem from the fact that T_{Rf} is lower than the actual (and unknown) T_R temperature.

2.3 Faceting–roughening of the first and second order

As described by Gibbs and Cahn [1–4], the free energy of the surface (or the internal interface) plays a crucial role in determining the two-dimensional phases of the surface and the corresponding phase transformations. These two-dimensional phases represent unfaceted (rounded) portions of the surface or interface, as well as crystallographically distinct facets. When both flat (faceted) and rounded (nonfaceted or rough) regions coexist on the surface or grain boundaries, they come together at the ridges, which can be either sharp (two different tangents) or smooth (one tangent). In the former scenario, the faceting–roughening phase transition is a first-order transformation. Conversely, in the latter case, it constitutes a second-order phase transformation (continuous). The gradual transition along smooth ridges between flat facets and rounded rough areas falls under the Pokrovsky–Talapov (PT) [67] or Andreev [68] universality class. Such second-order transitions have been observed on the surfaces of lead [56] and helium crystals [20, 69]. Typically, sharp ridges of the first order are observed at grain boundaries when transitioning from a faceted area to a rough (rounded) region [70–72].

In reference [73], a cylindrical molybdenum bicrystal was grown from the melt with coaxial grains misoriented by approximately 72° around the {110} axis, corresponding to the twin grain boundary $\Sigma 3$. While the geometry of these specimens is akin to that of the bicrystals created in references [70–72], the resulting shape of the grain boundary is markedly different. Figure 5 displays an EBSD micrograph depicting the cross-section of this bicrystal. The twin boundary $\Sigma 3$

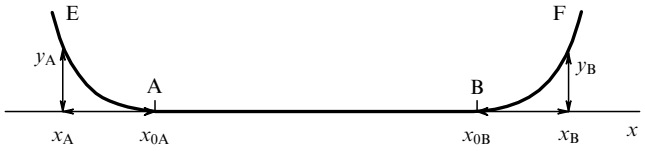

Figure 4. A diagram illustrating the quantification of curved regions in the grain boundary (GB) near the $(100)_{\Sigma 3CSL}$ facet. This diagram has been reproduced from [73] with the permission of the American Physical Society © 2004.

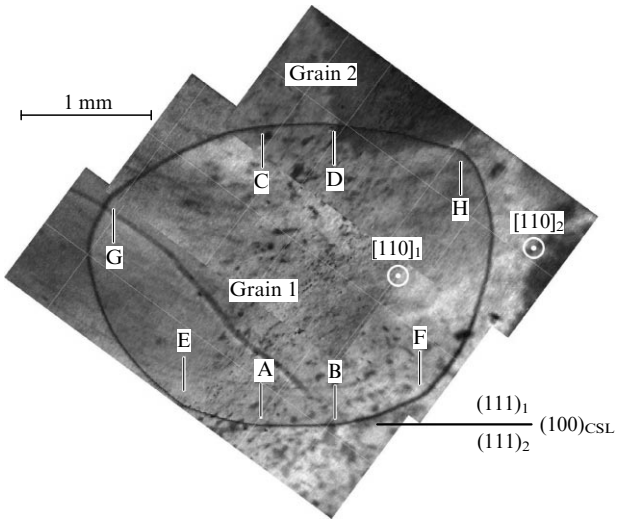

Figure 5. EBSD micrograph showing a segment of a molybdenum bicrystal perpendicular to the common tilt axis of two grains $[110]_1/[110]_2$. The planar facets $(100)_{\Sigma 3CSL}$ are situated between points A and B, and C and D, respectively. The GB sections between points A and C, as well as between D and B are rounded. At points E, F, G, and H, there are ridges of the first order delineating two rounded sections of the GB. This illustration has been adapted from [73] with permission of the American Physical Society © 2004.

appears predominantly rounded and features only two parallel planar facets, specifically $(111)_1||(111)_2$ symmetrical twin GBs, or $(100)_{CSL}$. The flat $(100)_{CSL}$ GB segments display smooth ridges (without discontinuities in the derivative) where they meet the rounded GB sections of the grain boundary zone (GB). This contact between the facet and the rough grain boundary resembles the configuration of facets on the surface of small lead balls [56]. In the proximity of the smooth facet edge, the shape of the curved interface follows a power law (refer to Fig. 4)

$$y = A(x - x_c)^{\beta} + \text{additional higher-order terms}. \quad (2)$$

The edge is positioned at a point with the x_c coordinate. The exponent β is called the critical exponent. The unfaceted GB region deviates from the $(100)_{CSL}$ plane following the x^{β} law with $\beta = 1.69 \pm 0.07$ on one side and $\beta = 1.72 \pm 0.07$ on the other side of the facet (refer to Fig. 6). In similar coaxial niobium bicrystals, the values observed were $\beta = 1.61 \pm 0.09$ and $\beta = 1.46 \pm 0.09$ [74].

There are two primary models used to predict the values of the critical exponent β. Andreev's approach to crystal shape determination, which relies on an mean field approximation and disregards fluctuations, employs a Landau-type decomposition of free energy near the roughening of second order [68]. This method predicts a critical exponent value of $\beta = 2$,

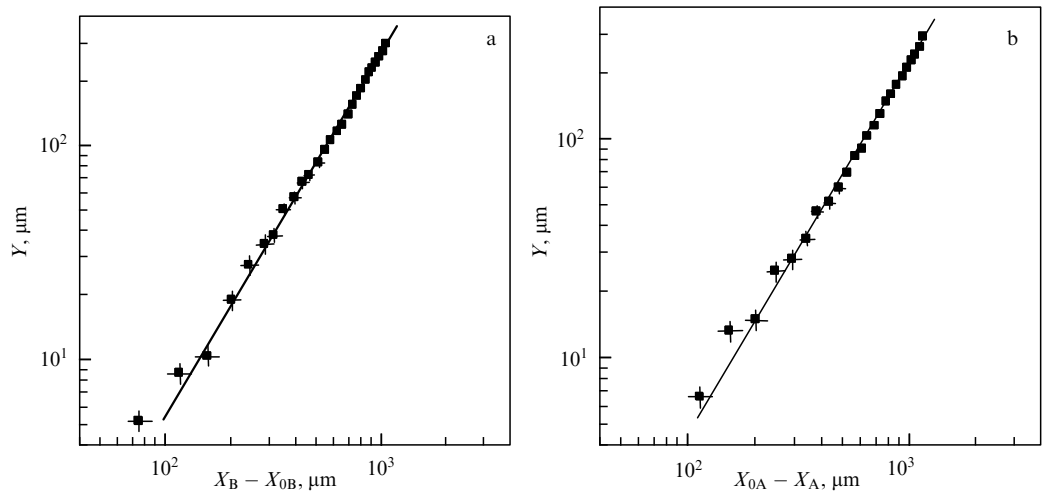

Figure 6. Profile of the rounded GB section near the $(100)_{\Sigma 3CSL}$ facet in scaling coordinates, shown for two different regions: (a) between points A and E (as depicted in Fig. 5), and (b) between points B and F. This diagram has been reproduced from [73] with permission from the American Physical Society © 2004.

indicating a quadratic law of effective step interactions. However, the experimental observation of $\beta = 2$ has never been confirmed. Pokrovsky and Talapov discussed the structure of a monolayer deposited on a periodic substrate that is incommensurate with the monolayer's periodicity [67]. The steps found on the interface resemble the boundaries that separate different commensurate regions in their model [67]. The theory set forth by Pokrovsky and Talapov predicts a critical exponent value of $\beta = 3/2$. Thus, we find for the roughening of second order for GB in molybdenum the values of β that are clearly lower than the prediction of the mean field theory and are more consistent with the Pokrovsky–Talapov (PT) theory. In the study of equilibrium surface particle shapes in lead, it was observed that the critical exponent β measured near the (111) face is not entirely universal and varies with the azimuth angle [56]. The values of β fall into two distinct groups: an average value around 1.7 (similar to the value for twin boundaries in molybdenum) and a value close to 3/2. The interaction between steps on the inner interface plays a role in determining the value of β. Scanning tunneling microscopy has revealed the presence of both (100) and (111) microfacets along these steps [75]. Higher β values are associated with steps along the (100) microfacets. For molybdenum's $\Sigma 3$ twin boundary, the difference between the measured and theoretical β values (according to the PT model) could be attributed to similar steps found on the grain boundary.

In Ref. [73], for the first time, not only was a second-order edge observed during the transition of a flat facet to a curved part of the grain boundary, but also the so-called first order ridges between two curved segments of the boundary were detected. In the EBSD micrograph in Fig. 5, characteristic kinks can be seen at points A and B, C and D. These kinks appear as if small-angle grain boundaries approach the primary boundary of $\Sigma 3$ at these locations and 'pull' it away from the center of curvature. However, Fig. 5 presents an EBSD micrograph rather than an SEM micrograph, as mentioned. This suggests that if small-angle boundaries were present at points A and B, C and D, they would be visible in the EBSD image, if their misorientation angle exceeded one and a half to two degrees. Furthermore, points A and B, C and D are crystallographically equivalent and are symmetrically positioned between two flat facets $[110]_1/[110]_2$. It would be expected that small-angle boundaries might approach the main boundary $\Sigma 3$ at various random locations. Therefore, in Fig. 5, it is indeed observed that there are four crystallographically equivalent first order ridges between curved segments of the boundary.

In Ref. [76], the authors documented the gradual disappearance of a flat facet at the tilt GB in zinc, flanked on both sides by first order ridges with curved sections of the boundary (depicted in Fig. 7a), as the temperature increased. Subsequently, a first order ridge between two curved sections of the GB (shown in Fig. 7b) emerged in its place. This observation was made on a flat zinc bicrystal grown from 99.999 wt.% pure zinc using a modified Bridgman technique. The bicrystal featured a tilt GB with a misorientation angle of 30°. Within this structure, two flat sections of the GB ran parallel to each other, creating a loop as illustrated in Fig. 7. Both the flat and curved portions of the boundary were perpendicular to the sample surface. The crystallographic axes in both grains were also perpendicular to the sample surface. The GB loop underwent gradual movement during annealing due to a constant capillary driving force determined by the average grain width. The morphology of the migrating grain boundary loop was analyzed within a temperature range of 633 to 683 K *in situ* under a hot state using a light microscope with polarized light. The temperature was maintained with a precision of ±0.5 K. Isothermal annealing was conducted in temperature ranges of 5 or 10 K, with each annealing period lasting either 120 or 180 s. The transition to the 'new' annealing temperature and sample stabilization occurred within a few seconds. The experiment was conducted in an atmosphere of high-purity nitrogen (99.999%) to prevent oxidation of the samples.

In Fig. 7c, the evolution of the shape of a moving GB is schematically depicted. At low temperatures, the GB shape features a facet that separates two first-order ridges with curved GB sections. This facet runs parallel to the closely packed lattice plane of the close coincidence sites lattice (CCSL) for the tilt boundary with a 30° misorientation angle. The aspect ratio c/a in zinc is irrational, where a represents the lattice period in the basis plane (0001), and c is the lattice period perpendicular to the plane (0001). As a

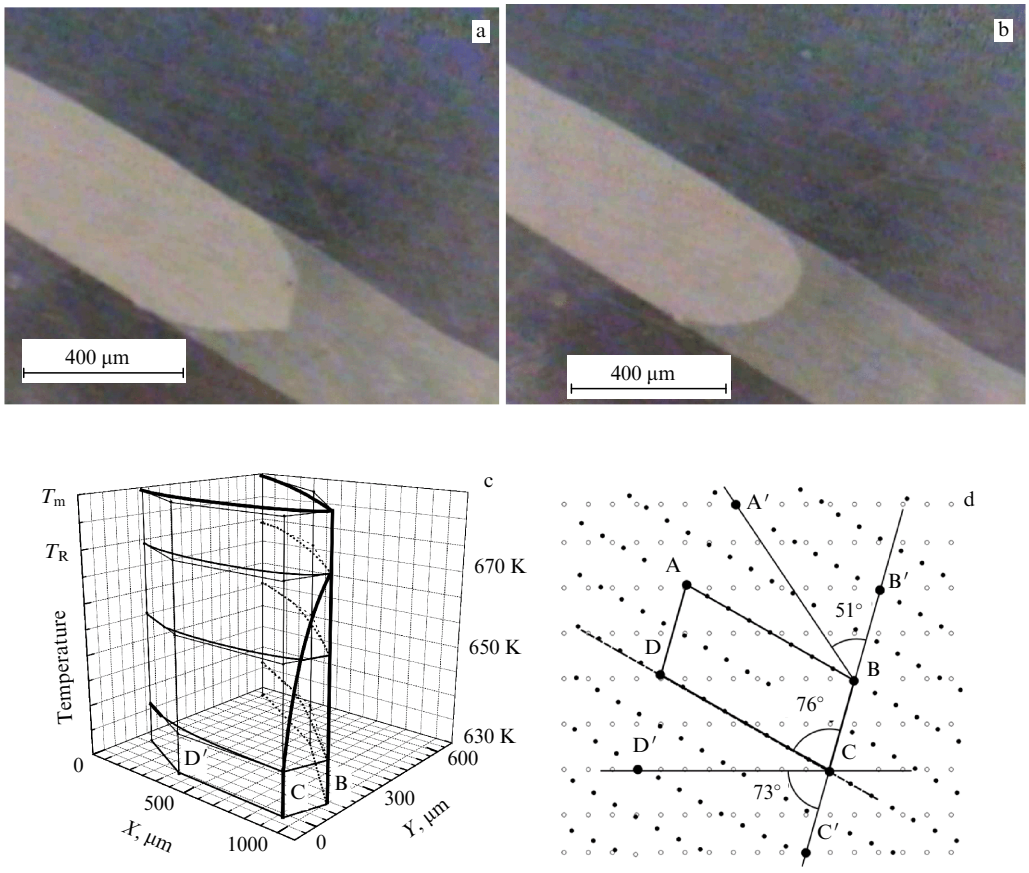

Figure 7. Light micrographs of a tilted GB with a 30° misorientation angle: (a) Lengthy facet on the GB loop and two first-order edges between the facet and a rounded GB at a temperature of 643 K below T_R. (b) First-order ridge between two curved GB sections at 678 K above T_R. (c) Diagram illustrating the impact of temperature on the shape of a GB loop, showcasing the presence of a facet between two first-order ridges at temperatures below T_R and a first-order ridge between two curved GB sections at temperatures above T_R. (d) Diagram of crystal lattices displaying the nodes of close coincidence sites lattice (CCSL) for GB in zinc perpendicular to the tilt axis with a 30° misorientation angle. Filled and empty circles indicate the locations of two misoriented zinc lattices. The CCSL nodes are denoted by large circles, and the inverse density of coincidence sites is $\Sigma = 15$. It also shows the unit cell of the corresponding CCSL (ABCD), the position of the basis plane (0001) for grain 2 (CD, shown as a dotted line), and the position of the CCSL plane BC parallel to the facet in the mobile part of the GB. The CCSL planes CD′ and BA′ are nearly parallel to the tangents to the lower and upper rounded parts of the GB at their intersections with the facet (below T_R) or with each other (above T_R). This illustration has been reproduced from [76] with the permission of the Elsevier © 2010.

result, an exact CSL is only present in zinc for the tilt angle involving rotation around the axis [0001]. In other scenarios, the so-called the close coincidence sites lattices (CCSL) need to be utilized [77, 78]. Interestingly, the tangents to the curved sections of the GB at points C and B (Fig. 2c, d) align parallel to the densely packed sections of the CCSL. With increasing temperature, the facet between points C and B vanishes (Fig. 2c), and instead of two first-order ridges transitioning to the curved boundary, a first-order ridge emerges between the curved sections of the GB. However, the orientation of the curved GB sections relative to each other is not arbitrary. The tangents along the edge of the curved sections remain parallel to the densely packed CCSL planes.

Faceting–roughening represents a reversible grain boundary phase transition. Initially observed during *in situ* heating and cooling in a transmission electron microscope, the roughening of Σ11 GB was noted at a temperature near the melting point of T_m in aluminum [79]. Similarly, experiments conducted *in situ* revealed that in zinc, the length of the GB facet gradually diminishes as the temperature rises, ultimately reaching zero at the point of roughening [72, 80]. Upon cooling below the temperature where the facet disappeared, the facet reemerges, albeit with some hysteresis of approximately 5 K [80]. Notably, CSL facets that form first-order ridges either with each other or with curved GB sections have been observed not only in metals but also in polysilicon [81, 82], gallium nitride [83], lead telluride [84], tungsten carbide [85], and textured rocks [86].

3. Grain boundary wetting phase transitions

3.1 Wetting of grain boundaries by the liquid and solid phases

Let us consider a polycrystalline sample located in the two-phase region S + L of the phase diagram (Fig. 8). In such a sample, there are grain boundaries (GBs) in the solid phase, as well as interphase boundaries between the melt and the solid phase (IBs). In these alloys, GBs in contact with the liquid phase form triple joints with interphase boundaries. If the energy of the two interphase boundaries of the solid and liquid phases $2\sigma_{SL}$ is higher than the energy of the grain boundary σ_{GB}, then a nonzero equilibrium contact wetting angle of $\theta > 0$ is formed in this case. This case is called partial (or incomplete) wetting of the grain boundary by the melt. If the energy of the two interphase boundaries of the solid and

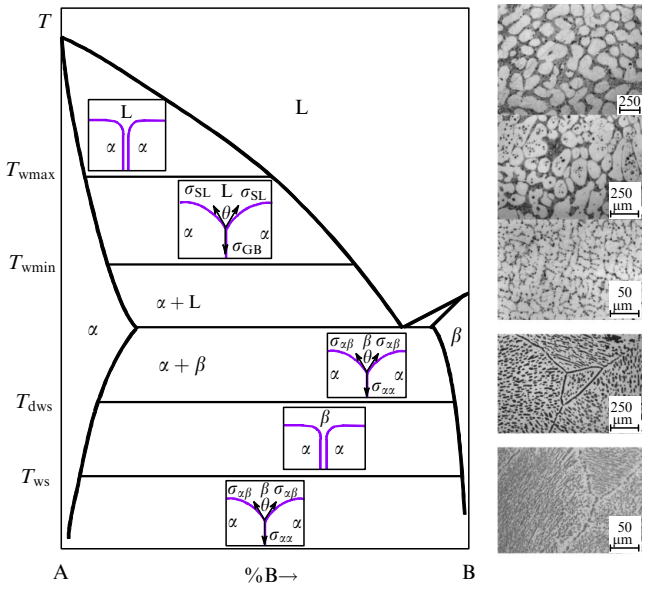

Figure 8. A schematic binary phase diagram for components A and B is presented to illustrate the wetting of grain boundaries. The thick solid lines depict phase transformations in the bulk material, while the thin solid lines represent the tie-lines of the GB wetting phase transition with either a melt or a second solid phase. Within the diagrams delimited by the solidus and liquidus lines, scenarios of complete wetting (upper part) and partial wetting (lower part) of grain boundaries with the liquid phase are depicted. Between the solvus lines for the α- and β-phases, the diagrams display cases of complete wetting (middle part) and partial wetting (upper and lower parts) of grain boundaries in the α-phase by the second solid phase β. The micrographs on the right side of the diagram illustrate the microstructure of Al–Mg samples subjected to treatment above the maximum wetting temperature of the boundaries, T_{wmax}. In the upper micrograph, all boundaries are completely wetted. Between the minimum and maximum temperatures, T_{wmin} and T_{wmax}, as shown in the middle micrograph, some boundaries are fully wetted while others are only partially wetted. Below the minimum temperature, T_{wmin}, illustrated in the lower micrograph, there are no completely wetted boundaries. Furthermore, the micrographs on the right side of the diagram also show the microstructure of Al–Zn samples annealed above the wetting temperature, T_{ws}, where Zn/Zn grain boundaries are fully wetted with the second solid phase (Al), as displayed in the upper micrograph. Conversely, when annealed below the T_{ws} temperature, as shown in the lower micrograph, all Zn/Zn grain boundaries are partially wetted with the (Al) phase. This diagram has been reproduced from [93] with the permission of MDPI Publishing House (open access) © 2021.

liquid phases $2\sigma_{SL}$ is less than the GB energy $2\sigma_{SL} < \sigma_{GB}$, then the contact angle should be zero $\theta = 0$. In this case, the GB will be replaced by a layer of liquid phase, and neighboring grains should be completely separated from each other by a thick layer of liquid. This is the complete wetting of the GB with the liquid phase. Usually, the contact angle θ between the GB and the melt decreases with increasing temperature [87]. The transition from incomplete to complete wetting causes the angle θ to decrease to zero at a certain temperature T_w. It is called the GB wetting transition temperature. The GB wetting phase transformation, similar to bulk phase transitions, can be of the first or second order [88]. For a phase transition of the first order, the derivative $d\theta/dT$ of the wetting angle θ with respect to temperature T has a discontinuity at T_w [87, 88]. It changes abruptly from a certain finite value to zero [87, 88]. For a phase transition of the second order, $d\theta/dT$ decreases continuously with increasing temperature and becomes zero at T_w without a jump [87]. The GB energy σ_{GB} strongly depends on the misorientation angle φ and the orientation angle ψ of the grain boundaries [43]. At certain values of the angles φ and ψ, the GB energy σ_{GB} has minima [89]. The higher the σ_{GB}, the smaller the contact angle θ at the triple junction of the grain boundary with the melt. The range of σ_{GB} variety in polycrystals is wide, therefore, at a certain temperature in a two-phase polycrystal, there is a wide range of values of θ. As the temperature increases, the wetting angles for different boundaries decrease at different rates. The final values of T_w are different for GB with different values of σ_{GB}.

The microstructures of two-phase binary Al–Mg polycrystals are depicted as an illustration in the upper right part of Fig. 8. Two wetting tie-lines for grain boundaries (GBs) are observed in the phase diagram. The first of these tie-lines, occurring at a temperature of T_{wmin}, marks the transition from partial to complete wetting for GB with the highest σ_{GB} value. Below T_{wmin}, the polycrystal is unable to contain fully wetted GBs, having only partially wetted GBs with $\theta > 0$. As temperatures exceed T_{wmin}, the first fully wetted GBs emerge in the polycrystal. Subsequently, as the temperature rises further, the percentage of fully wetted GB gradually increases, reaching unity at T_{wmax}, illustrated in the figure within the (S) + (L) region as the second tie-line. Beyond this T_{wmax} threshold, all GBs are completely wetted. In this domain, individual grains essentially 'float' in the melt and cannot touch other solid crystallites. The presence of 'dry' grain boundaries above T_{wmax} is thermodynamically unfavorable; hence, beyond the T_{wmax} threshold, all solid grains are isolated from each other by relatively thick liquid layers. Consequently, additional lines manifest in the (S) + (L) region for the GB wetting phase transition, usually not depicted in conventional phase diagrams. Therefore, the microstructure of the polycrystal following solidification will differ based on the solidification process.

Now, let's explore another two-phase region located at the lowermost part of the phase diagram depicted in Fig. 8. In this area, two solid phases, namely α and β, exist in equilibrium. These phases represent solid solutions, with the α-phase containing component (B) within component (A), and the β-phase containing component (A) within component (B). Within a two-phase polycrystal, there exist three distinct types of internal interfaces. The first type comprises grain boundaries within the α solid solution, the second type involves grain boundaries within the β solid solution, and the third encompasses the interphase boundaries between the α and β phases. These three interface types can give rise to four kinds of triple junctions (TJs). The initial two are triple junctions involving α/α and β/β grain boundaries. The third and fourth types involve triple junctions where α/α GBs intersect with α/β interphase boundaries, and β/β triple junctions intersect with α/β interphase boundaries, respectively.

If we analyze the energy relations between the energies of the grain boundaries $\sigma_{\alpha\alpha}$, $\sigma_{\beta\beta}$ and the energy of the interface $\sigma_{\alpha\beta}$, we will also be able to detect the phenomena of complete and incomplete wetting. From a thermodynamic point of view, they are similar to the GB wetting with a liquid phase (as mentioned earlier). However, in the case of two solid phases, the wetting phase is also solid. Let us consider the contact of the α/α GB and the α/β interphase boundary. If the energy of the grain boundary $\sigma_{\alpha\alpha}$ — is less than the energy of the two interphase boundaries $2\sigma_{\alpha\beta}$, $\sigma_{\alpha\alpha} < 2\sigma_{\alpha\beta}$, then the contact angle at the triple junction is nonzero $\theta > 0$ (see the diagram at the bottom of the Fig. 8). In this case, incomplete wetting of

the α/α GB by the second phase β occurs. If the energy of the two interphase boundaries $2\sigma_{\alpha\beta}$ is less than the energy of the grain boundary $\sigma_{\alpha\alpha}$, $\sigma_{\alpha\alpha} > 2\sigma_{\alpha\beta}$, then the α/α GB will be replaced by a layer of β phase, and the wetting angle will be zero, $\theta = 0$. In this case, the α/α GB is completely wetted by the intermediate layer of the β-phase.

Up to this point, we had not observed any significant differences between the GB wetting situation by the second solid phase and the liquid phase. However, there are no grain boundaries in the liquid phase, while in the second phase β they are present in the phase diagram under consideration. Therefore, a symmetrical situation arises if we consider the grain boundary in the β-phase, which is in equilibrium contact with the α-phase. If the energy of the GB $\sigma_{\beta\beta}$ is less than the energy of the two interphase boundaries $2\sigma_{\alpha\beta}$, $\sigma_{\beta\beta} < 2\sigma_{\alpha\beta}$, then there will be a nonzero contact angle $\theta > 0$ at their triple junction (see the diagram at the bottom of the Fig. 8). In this case, incomplete wetting of the β/β GB with the second solid phase α occurs. If the energy of the two interphase boundaries $2\sigma_{\alpha\beta}$ is less than the energy of the grain boundary $\sigma_{\beta\beta}$, $\sigma_{\beta\beta} > 2\sigma_{\alpha\beta}$, then the GB β/β will be replaced by a phase layer α, and the wetting angle will be zero, $\theta = 0$. In this case, we are dealing with complete wetting of the GB by the β/β intermediate layer of the α-phase.

Furthermore, if the criteria for complete wetting are met simultaneously for both β/β and α/α boundaries, namely $\sigma_{\alpha\alpha} > 2\sigma_{\alpha\beta}$ and $\sigma_{\beta\beta} > 2\sigma_{\alpha\beta}$, then no grain boundaries can coexist in thermodynamic equilibrium within a two-phase $\alpha + \beta$ polycrystal. Consequently, the two-dimensional section of this polycrystal will exhibit a topological resemblance to a chessboard. In such a polycrystal, there will be no α/α and β/β GBs present, and only α/β interphase boundaries remain.

There is another important difference between the GB wetting with a second solid phase and a melt. In the case of wetting with a liquid phase, the free energy of the unit area of the GB σ_{GB} decreases with increasing temperature, and usually more slowly than the energy of the interface between the solid and liquid phases σ_{SL}. This is due to the higher entropy of the liquid phase compared to the solid phase. As a result, the GB wetting angle θ with a melt always decreases with increasing temperature until it reaches zero value $\theta = 0$ at the transition temperature. Upon further heating, the angle θ remains zero until the sample has completely melted. This behavior of the wetting angle has been observed in many binary systems [87, 88].

In the case of GB wetting with the second solid phase, there is no such obvious difference in the dependence of the energy of grain boundaries $\sigma_{\alpha\alpha}$, $\sigma_{\beta\beta}$ and interphase boundaries $\sigma_{\alpha\beta}$ on temperature. In this case, the wetting angle θ can either increase or decrease with increasing temperature. For example, in aluminum-magnesium and aluminum-zinc alloys, a change in the wetting angle was observed, similar to wetting with a liquid phase. Thus, in the system, the contact angle between the grain boundaries in aluminum (Al)/(Al) and the second solid phase Al_3Mg decreased with increasing temperature until it reached zero at the T_{ws} transition temperature, after which it occurred complete wetting [90]. In the case of the aluminum–zinc system, on the contrary, the contact angle between the grain boundaries of aluminum and solid zinc decreased with decreasing temperature until it reached zero at the T_{ws} transition temperature from partial wetting of grain boundaries to complete one [91].

Furthermore, it is noteworthy that the temperature dependencies of the grain boundary energy $\sigma_{\alpha\alpha}(T)$ and the doubled energy of the interphase boundaries $2\sigma_{\alpha\beta}(T)$ may intersect twice during a temperature variation. In this scenario, an intriguing phenomenon can occur, wherein the wetting angle decreases as the temperature increases towards the transition temperature to complete wetting, denoted as T_{ws}. Subsequently, within a specific temperature range, all grain boundaries in one solid phase become wetted by intervening layers of the second solid phase. As the temperature continues to rise, a second transition takes place where the wetting vanishes at the temperature T_{dws} Above this temperature, the grain boundaries in the α-phase once again remain incompletely wetted by the second β solid phase. This phenomenon has been documented, for instance, in the copper–indium system [92].

The schematic Fig. 8 illustrates tie-lines in the two-phase $\alpha + \beta$ region for wetting at a temperature of T_{ws} and for 'drying' (dewetting) at a temperature of T_{dws}. It is important to note that the diagram presented is highly simplified. In previous discussions on liquid phase wetting, it has been observed that all grain boundaries in a polycrystal possess varying energy levels σ_{GB}. For each value of this energy σ_{GB}, there exists a corresponding wetting phase transition temperature T_w. Consequently, the tie-lines of T_{ws} and T_{dws} should actually be splitted into a spectrum of lines. For each temperature, it is necessary to depict not just one line, but at least two lines representing the maximum and minimum values of T_{ws} and T_{dws}, respectively [90].

Wetting of grain boundaries with a solid phase introduces another level of complexity. This complexity stems from the greater anisotropy typically observed at interphase boundaries between two solid phases compared to those between a solid and a melt. Hence, in calculating the contact angle θ, it becomes essential to consider not only the energies of the grain boundaries and interfacial boundaries but also their angular derivatives, known as the Herring torque. The magnitude of this torque diminishes as temperature rises.

Up to this point, we have examined the thermodynamic prerequisites for complete and incomplete wetting of grain boundaries in a solid phase by intermediate layers of another solid phase. However, there exists a notable kinetic contrast with liquid-phase boundary wetting. When containing a liquid phase, the system quickly attains equilibrium due to the rapid mass transfer within the melt. In contrast, the wetting process with a second solid phase unfolds at a far slower pace, necessitating significantly lengthier annealing durations in experiments. These extended periods may span many months to establish thermodynamic equilibrium effectively.

3.2 Grain boundary wetting phase transitions of first and second order

When a drop of liquid rests on a solid surface, two scenarios may unfold. Complete wetting occurs when the liquid spreads uniformly across the surface, leading to a zero contact angle between the liquid and the solid material. In contrast, when a liquid drop maintains a specific contact angle with the solid rather than spreading, we observe partial (or incomplete) wetting. Cahn [94] and Ebner and Saam [95] were among the first to propose that the transition from partial to complete wetting could happen with increasing temperature, representing an actual 2D phase transformation on the external surface. Cahn further suggested that a wetting phase transition should take place in the three-phase region of the phase diagram near the critical point T_c, where the two phases α'

and α'' become indiscernible. This is rationalized by the idea that if the α' and α'' phases become identical at the critical temperature T_c, and the β-phase remains constant, there will always exist a temperature T_w close enough to the critical T_c, above which the energy $\sigma_{\alpha\alpha}$ of the α'/α'' interface will be lower than the energy $\sigma_{\alpha\beta}$ of the α'/β interface (or α''/β). Comprehensive reviews on studies focusing on phase transitions during wetting are available in [96–100].

As previously discussed, the transition from incomplete to complete wetting, and vice versa, can be observed not only on external surfaces but also on internal interfaces like intercrystalline or grain boundaries. For this transition to occur, the energy associated with the two interphase interfaces between the solid and liquid phases, $2\sigma_{SL}$, must become less than the energy of the grain boundary, $2\sigma_{GB}$. Cahn's concept [94] served as the catalyst for experimentally detecting phase transformations during grain boundary wetting, starting with studies on polycrystals like Zn–Sn, Zn–Sn–Pb, and Ag–Pb [101, 102]. Subsequently, many earlier experimental results were reevaluated through this lens, revealing multiple indications of wetting phase transformations in polycrystals such as Zn–Sn, Al–Cd, Al–In, Al–Pb [101–103], and W–Ni, W–Cu, W–Fe, Mo–Ni, Mo–Cu, Mo–Fe [104]. The initial precise measurements of the temperature-dependent contact angle of the grain boundary with the melt were conducted using individual grain boundaries in specially grown bicrystals within the Cu–In [105], Al–Sn [106], and Zn–Sn [107] systems. Additionally, Cahn predicted that the wetting transition line (tie-line) in the two-phase region extends into the single-phase region (solid solution) as a pre-wetting line [94].

Between the pre-wetting line and the solubility limit line of the solid solution, there exists a thin layer on the surface that exhibits liquid-like properties and is unstable in volume. Experimental evidence supporting the existence of these pre-wetting (or pre-melting) layers has been identified at grain boundaries in systems like Fe–Si–Zn [108, 109], Cu–Bi [110], Al–Zn [111], and in semiconductors such as AlN doped with yttrium oxide [112], La–$SrTiO_3$ [113], ZnO doped with bismuth oxide [114, 115], and $CaSi_3N_4$ doped with calcium [116]. The occurrence of phase transformations during wetting and pre-wetting (pre-melting) significantly alters critical properties of the grain boundary zone, including the diffusion coefficient [107–110], mobility [117], strength [110, 118], segregation [110, 119–121], and conductivity [112–116, 122]. The wetting phenomena in grain boundaries play a pivotal role in processes like liquid-phase sintering of metals and ceramics [123, 124], the manufacturing of semi-liquid alloys [125], thixotropic casting [126], and in the operation of heat exchanger tubes containing liquid metal in nuclear power plants [127], among other applications.

All the phase transformations mentioned concerning wetting on external surfaces and grain boundaries are classified as first-order transitions. This indicates a discontinuity (jump) in the first derivative of the surface energy (or GB energy) at a specific temperature, T_w. However, it is also conceivable to have higher-order wetting transitions where the higher derivatives of the surface energy (or GB energy) exhibit discontinuities. In other words, while the first derivative of the surface energy (or GB energy) remains continuous at T_w, the second derivative or higher-order derivatives experience discontinuities. Phase transitions involving continuous wetting of surfaces (referred to as wetting of the second order) were theoretically predicted in [128–130] and have been the subject of extensive theoretical exploration for a considerable period [131–133], with a comprehensive overview available in [100]. Experimentally, the continuous wetting phase transitions have been observed when alkanes interact with methanol, water, or brine in liquid/solvent systems, which holds practical significance, especially in the realm of oil production [134–139]. A continuous and divergent increase in the thickness of the alkane layer on an aqueous or salt substrate has been noted due to long-range critical wetting propelled by long-range van der Waals forces. This phenomenon typically follows a first-order transition from a thin layer to a thicker one in the adsorbed alkane layer, resulting in the formation of a mesoscopic film on the surface of water or brine. These observations have enhanced our comprehension of interfacial processes among different liquids, supported by both experimental findings and theoretical investigations [140–146]. Nevertheless, the primary source for studying continuous wetting transformations for an extensive period remained the data obtained from a limited number of similar liquid systems [134–139, 147, 148]. In the conclusions of an extensive review [100] on these phenomena, there was an expressed optimism in uncovering similar results in varied systems, including those involving a solid substrate.

The wetting phase transformations involving a solid substrate, particularly grain boundaries in a solid bicrystal, were initially observed in [88]. This study investigated the GB wetting processes of both the first and second order on in the Al–Zn system utilizing individual GB within specially grown aluminum and zinc bicrystals. Referring to the Al–Zn bulk phase diagram (Fig. 9), it is evident that this system falls under the category of 'classical' systems with a critical point for a binary solid solution, known as the monotectoid transformation [111]. Experiments conducted on Al–Zn polycrystals revealed that within the (Al) + L two-phase region, phase transformations involving the GB wetting in aluminum by a zinc-containing melt took place. The temperature $T_{wGB0\%} = 440\,^{\circ}C$ on the diagram signifies the wetting temperature for a GB exhibiting maximum energy σ_{GBmax}. Below $T_{wGB0\%} = 440\,^{\circ}C$, fully wetted GBs are absent in Al–Zn

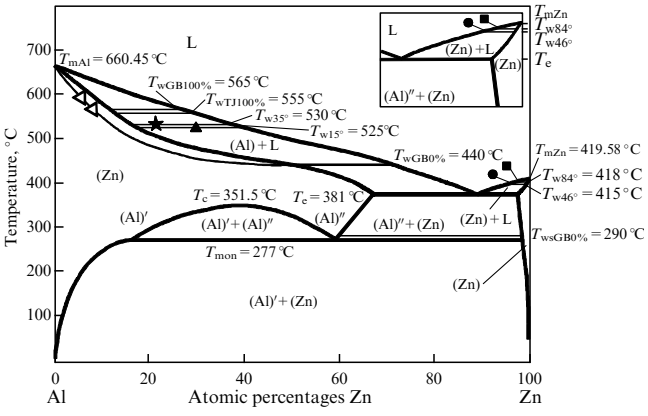

Figure 9. The Al–Zn phase diagram constructed using data from [91, 111, 149–153]. In the diagram, thick lines represent bulk phase transformations [152], while thin lines represent phase transformations at grain boundaries [91, 111, 149, 150]. The open triangles represent the TEM and DSC data for the pre-wetting line on the GB [150, 151]. Filled asterisks, triangles, circles, and squares depict the wetting phase transition temperatures [88]. The inset highlights the angle of the diagram, emphasizing high concentrations of zinc. This drawing is reproduced from [88] with permission from the American Physical Society © 2008.

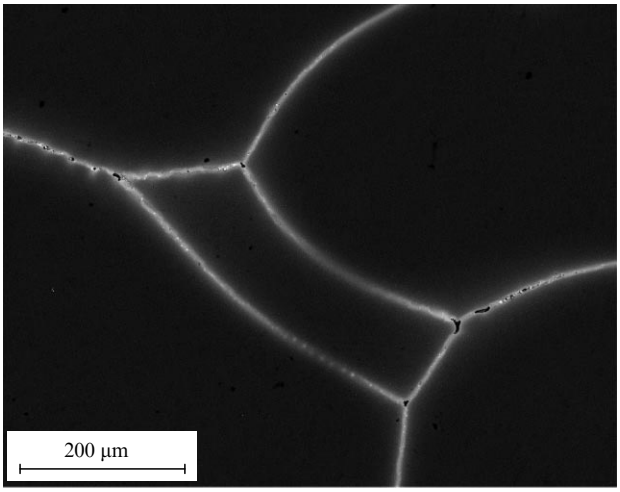

Figure 10. SEM micrograph of the Al—5 at.% Zn alloy annealed at $T = 620\,^{\circ}\mathrm{C}$ (above $T_{\mathrm{wGB100\%}} = 565\,^{\circ}\mathrm{C}$). In the micrograph, the (Al) matrix appears black, while the solidified melt rich in zinc appears white. This illustration is reproduced from [88] with permission from American Physical Society © 2008.

polycrystals. Conversely, temperatures exceeding $T_{\mathrm{wGB100\%}} = 565\,^{\circ}\mathrm{C}$ result in the wetting of all high-angle GBs in (Al) by the melt (Fig. 10) [111, 149]. $T_{\mathrm{wGB100\%}}$ represents the wetting temperature for GB with a minimum energy σ_{GBmin}. Notably, between $T_{\mathrm{wGB0\%}}$ and $T_{\mathrm{wGB100\%}}$ within the (Al) + L region, there exist wetting tie-lines for GB characterized by an intermediate energy value σ_{GB}, where $\sigma_{\mathrm{GBmax}} > \sigma_{\mathrm{GB}} > \sigma_{\mathrm{GBmin}}$. The triple joints of the GB become fully wetted at a temperature of $T_{\mathrm{wTJ100\%}} = 555\,^{\circ}\mathrm{C}$, which is lower than $T_{\mathrm{wGB100\%}}$ [149]. Per the generalized Cahn phase diagram, the wetting phase transition tie-lines within the two-phase region (Al) + L extend into the single-phase region (Al) as pre-wetting phase transition lines. Figure 9 illustrates only one pre-wetting line for $T_{\mathrm{wGB0\%}}$. Experimental data confirming the presence of a thin quasi-liquid phase layer on the GB between the GB pre-wetting line and the bulk solidus line were obtained using transmission electron microscopy (TEM) [150] and differential scanning calorimetry (DSC) [151]. It is also worth noting that the second solid phase (Al) can wholly wet GB in polycrystals (Zn), and conversely, the second solid phase (Zn) can completely wet GB in polycrystals (Al) [91].

The (Zn) phase represents a zinc-based solid solution of Zn+Al. The phases $(\mathrm{Al})'$ and $(\mathrm{Al})''$ denote isomorphic solid solutions based on Al with low and high zinc content, respectively, occurring below the critical point $T_{\mathrm{c}} = 351.5\,^{\circ}\mathrm{C}$. Below the temperature $T_{\mathrm{wGB0\%}} = 290\,^{\circ}\mathrm{C}$ in polycrystals (Zn)+$(\mathrm{Al})''$, there are no GBs in zinc completely wetted with the solid phase $(\mathrm{Al})''$. Above $T_{\mathrm{wGB0\%}}$, GB in zinc, completely wetted by the solid phase (Al), form polycrystals (Zn) + (Al). The proportion of fully wetted GBs in zinc rises as the temperature increases, reaching approximately 30% at the eutectic temperature $T_{\mathrm{e}} = 381\,^{\circ}\mathrm{C}$. Most GBs in zinc remain incompletely wetted with the solid phase $(\mathrm{Al})''$ at T_{e}; as a result, no $T_{\mathrm{wsGB100\%}}$ tie-line exists in the two-phase region $(\mathrm{Al})'' + (\mathrm{Zn})$ of the Al–Zn phase diagram. Experiments have demonstrated that the $(\mathrm{Al})'$ phase with a low zinc concentration falls short of complete wetting the GB in zinc within the $(\mathrm{Al})'+(\mathrm{Zn})$ two-phase region when the temperature is lower than the monotectoid transformation temperature

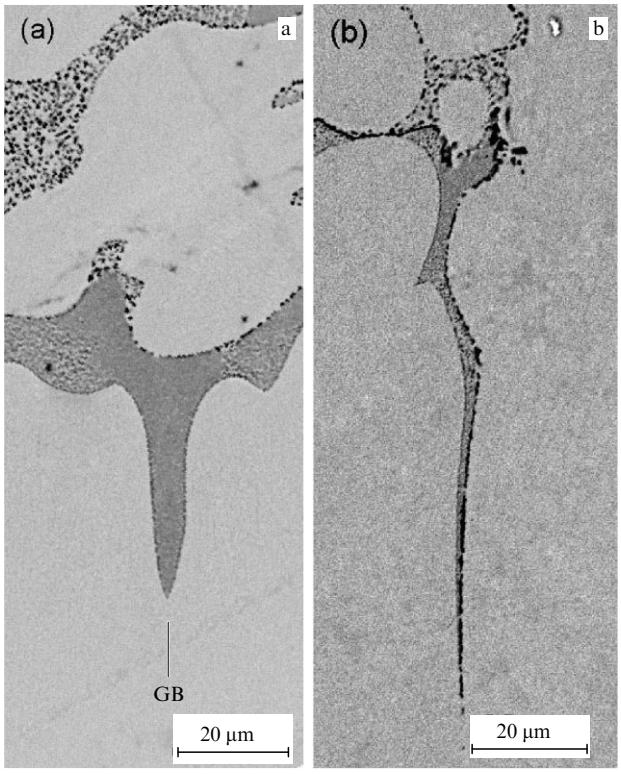

Figure 11. The wetting contact angle between the tilt boundary with a misorientation angle of $\theta = 46^{\circ}$ in a zinc bicrystal (lower section of the SEM micrographs, light color) and a melt containing aluminum (upper section of the SEM micrographs, gray color) at (a) 394 °C and (b) 408 °C. The illustration is reproduced from [88] with permission from the American Physical Society © 2008.

$T_{\mathrm{mon}} = 277\,^{\circ}\mathrm{C}$ [91]. The same holds true for the opposite side of the two-phase region $(\mathrm{Al})'+(\mathrm{Zn})$, where the solid phase (Zn) is also incapable of fully wetting the GB in the $(\mathrm{Al})'$ phase [153].

In [88], flat bicrystals of aluminum and zinc of high purity were grown. They contained two tilt GB ⟨110⟩ with misorientation angles $\varphi = 15^{\circ}$ and 35° in aluminum and three tilt GB with misorientation angles $\varphi = 11.5^{\circ}$, 46° and 84° in zinc. These samples were annealed in evacuated quartz ampoules at various temperatures. Figure 11 shows, as an example, the wetting angle θ formed by a melt containing aluminum on a zinc alloy with a misorientation angle $\varphi = 46^{\circ}$ after annealing at 394 °C and 408 °C. The wetting contact angle θ changes with temperature changes during the experiments. For aluminum bicrystals, the contact angle starts at approximately $\theta = 80^{\circ}$, decreases with increasing temperature, and reaches 0° at certain values of $T_{\mathrm{w15^{\circ}}} = 525\,^{\circ}\mathrm{C}$ for $\varphi = 15^{\circ}$ and $T_{\mathrm{w35^{\circ}}} = 530\,^{\circ}\mathrm{C}$ for $\varphi = 35^{\circ}$. Above the specified values of $T_{\mathrm{w15^{\circ}}}$ and $T_{\mathrm{w35^{\circ}}}$, the contact angle remains zero. The temperatures $T_{\mathrm{w15^{\circ}}}$ and $T_{\mathrm{w35^{\circ}}}$ are in a certain range between the temperatures $T_{\mathrm{wsGB0\%}}$ and $T_{\mathrm{wsGB100\%}}$ measured in polycrystals (see Fig. 9). The dependence of the contact angle $\theta(T)$ for both types of aluminum bicrystals is convex. The first derivative of the dependence $\theta(T)$ (and, consequently, the GB energy) experiences a discontinuity at the temperature $T_{\mathrm{w15^{\circ}}}$ and $T_{\mathrm{w35^{\circ}}}$. The predicted convex shape and discontinuity of the temperature derivative are related to wetting phase transitions of the first order. For zinc bicrystals, the wetting contact angle begins to change at approximately $\theta = 80^{\circ}$ [98], decreases with increasing tem-

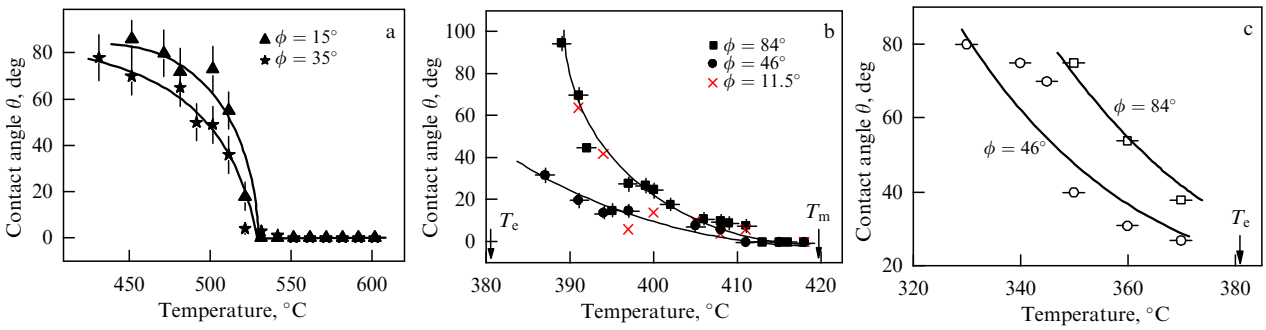

Figure 12. Temperature dependencies of the wetting contact angle θ for (a) GB in aluminum in contact with a melt enriched in zinc; (b) GB in zinc in contact with a melt enriched in aluminum; (c) GB in zinc in contact with a solid phase (Al)″. The illustration has been reproduced from [88] with permission from the American Physical Society © 2008.

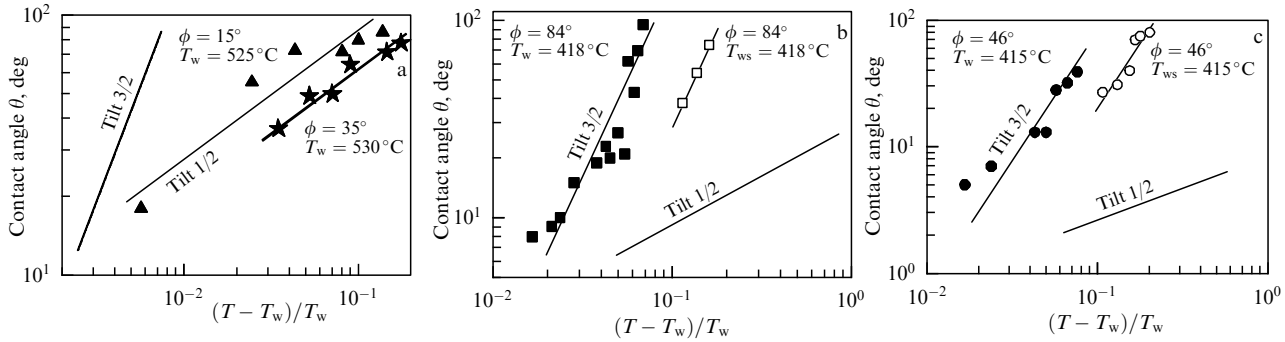

Figure 13. Temperature dependencies of the wetting angle θ (represented by the same symbols as in Fig. 12) in scaling coordinates. The diagram is reprinted from [88] with permission from the American Physical Society © 2008.

perature, and reaches 0° at $T_{w46^\circ} = T_{w11.5^\circ} = 415\,^\circ$C for $\varphi = 46^\circ$ and $\varphi = 11.5^\circ$ and at $T_{w84^\circ} = 418\,^\circ$C for $\varphi = 84^\circ$. At temperatures above the specified values T_{w46°, $T_{w11.5^\circ}$ and T_{w84° the contact angle remains zero. The dependence of the contact angle $\theta(T)$ for all three types of zinc bicrystals is concave. The first temperature derivative of the dependence $\theta(T)$ (and, correspondingly, of the GB energy) remains continuous at the values T_{w46°, $T_{w11.5^\circ}$ and T_{w84°. The predicted concave shape $\theta(T)$ and the continuity of the temperature derivative are related to second-order wetting transitions [98].

In the scenario of solid-phase wetting of zinc grain boundaries, the wetting angle initiates at approximately $\theta = 80^\circ$, decreases as the temperature rises, and stabilizes at $\theta = 37^\circ$ for grain boundaries with misorientation angle $\varphi = 46^\circ$ and $\theta = 28^\circ$ for grain boundaries with $\varphi = 84^\circ$ at a temperature of $T = 370\,^\circ$C. In essence, both examined grain boundaries fall under the category of grain boundaries that retain some wetting with the second solid phase (aluminum) below T_e. Notably, the relationship $\theta(T)$ for both zinc grain boundaries exhibits concavity. As previously noted, the concave profile signifies wetting transitions of the second order (continuous) [98].

The convex shape and discontinuity in the temperature derivative of $\theta(T)$ are typical characteristics of GB wetting phase transformations during [86, 101–106]. However, the concave shape and continuous temperature derivative for $\theta(T)$ were observed for the first time in the wetting of GB in [88]. The theory also predicts various critical parameters, specifically 1/2 for first-order transitions and 3/2 for continuous wetting transitions [98]. To determine the critical parameters, the measured dependencies of $\theta(T)$ (Fig. 12) are presented in Fig. 13 in scaling coordinates $\log\theta - \log((T - T_w)/T_w)$. The data for all GB systems correspond closely to a slope of 1/2 (Fig. 13a). Additionally, a line with a slope of 3/2 is included for comparison. In essence, the scaling condition for first-order transitions is met for the wetting of GB in aluminum with a zinc-enriched melt. A critical value of 1/2 for the GB wetting transition was also observed for tilt GBs in aluminum wetted with a tin-rich melt [86]. The temperature dependencies $\theta(T)$ for two GB systems with different misorientation angles exhibited convex shapes, and a discontinuity in the temperature derivative of $\theta(T)$ was similarly noted [86].

On the contrary, the data for grain boundaries in zinc exhibit a good agreement with a 3/2 slope (depicted in Figs 13b and c). This observation holds true for grain boundary wetting with both the liquid phase (represented by filled symbols) and the second solid phase (indicated by open symbols). The extrapolated values $T_{ws46^\circ} = 415\,^\circ$C and $T_{ws84^\circ} = 410^\circ$ were utilized to facilitate GB wetting in zinc with the solid phase (Al)″. Lines with a slope of 1/2 are included for comparison. In essence, the scaling condition for a continuous transition is satisfied when GB in zinc is wetted with both a melt enriched in aluminum and a solid phase (Al)″.

Experiments with polycrystalline Zn–5% Al alloys have shown that the first grain boundaries in zinc are completely wetted with the solid phase (Al)″ at a temperature of $T_{wsGB0\%} = 290\,^\circ$C (see Fig. 9) [91]. However, at the eutectic temperature of $T_e = 381\,^\circ$C, only about 30% of all GB zinc is wetted. These GB have the highest energy among all GB in a zinc polycrystal. The boundaries of zinc grains with low energy (such as twin GB) remained incompletely wetted at T_e. In alloys with a high aluminum content, all high-angle grain boundaries are wetted with melt at temperatures above $T_{wGB100\%} = 565\,^\circ$C (see Fig. 9) [149]. The minimum tempera-

ture of the phase transition during wetting of grain boundaries for aluminum is $T_{wGB0\%} = 440\,^{\circ}C$ (see Fig. 9) [111]. The wetting phase transition temperatures for the GBs grown in [88] are $T_{w35^{\circ}} = 530\,^{\circ}C$ and $T_{w15^{\circ}} = 525\,^{\circ}C$, which is close to the maximum wetting temperature and far from the minimum. The energy difference between grain boundaries with misorientation angles of 15° and 35° is greatest for boundaries with a slope of $\langle 110 \rangle$ [154]. This means that all tilt grain boundaries have a relatively low energy, comparable to general grain boundaries in a polycrystal. Therefore, it is not surprising that the three zinc GBs grown in [88] remain partially wetted at T_e. This is especially important because the grain boundaries with an inclination of 84° are very close to the twin grain boundaries, which have the lowest energy among all grain boundaries in zinc. Therefore, the T_{we} values for such grain boundaries were estimated using extrapolation to temperatures above T_e (Figs.12b, 13b, c).

If the concave shape and the continuous temperature derivative for $\theta(T)$ (depicted in Figs 12b and c) undeniably suggest that the GB wetting transition in zinc-rich samples occurs continuously, then the critical index of 3/2 (as shown in Figs 13b and c) warrants a more in-depth discussion. Specifically, the 3/2 index is anticipated for critical wetting in systems where wetting behavior is influenced by long-range forces, particularly the dispersion force, which is often disregarded [98, Section IV.B]. However, it is commonly believed that wetting in metal systems is governed by short-range forces rather than by the dispersive force, and prevailing wetting theories do not foresee a universal critical index of 3/2 for such systems [98, Section III.B-D]. Consequently, the observed 3/2 index could either be coincidental or indeed signify that the wetting of GB in zinc, combined with an aluminum-containing melt, is influenced by long-range forces. The latter possibility would certainly be more intriguing. This hypothesis can be experimentally validated. Given that the dispersion force is also weak in metals, it is conceivable that the GB in zinc will exhibit considerable thickness (several tens of atomic layers) just below the wetting temperature, akin to mesoscale alkane films in aqueous environments [147]. The existence of 'thick' prewetting films on GBs has been substantiated by both direct and indirect experiments in metal systems such as high aluminum content Al–Zn alloys [150, 151, 153], Cu–Bi alloys [110, 155], or Fe–Si–Zn alloys [107–109]. Directly observing these 'thick' GBs in Zn–Al alloys with high zinc content positioned just below the wetting temperature would compellingly demonstrate the significance of long-range forces in the GB wetting in metal systems.

Thus, in [88], a transition was experimentally observed in the Al–Zn system from a first-order phase transition for GB wetting on the aluminum-rich side of the Al–Zn diagram to continuous GB wetting on the zinc-rich side. In [156], an analysis of multilayer adsorption on substrates with attractive forces was conducted. Various scenarios involving the energies of substrate-liquid interaction and interatomic interaction within the liquid phase were investigated. Theoretical predictions indicated that in the presence of strong substrate-liquid interaction and weak liquid-liquid interaction, wetting would manifest as a first-order transition. Conversely, if the substrate-liquid interaction weakened, the wetting transition could become continuous [156]. The interatomic interaction in a metal is intrinsically linked to its melting point. Drawing a parallel to the theory proposed in [156], aluminum, with its higher melting point ($T_{mAl} = 660.45\,^{\circ}C$), can be likened to a 'stronger' substrate, while zinc ($T_{mZn} = 419.58\,^{\circ}C$) can be considered weaker. The shift from grain boundaries in aluminum to those in zinc signifies a shift from first-order to continuous wetting. Similar to the discussion regarding the critical index of 3/2, [156] primarily focuses on long-range interactions between substrates, which may not always be directly applicable to metal systems. Hence, future experiments aimed at identifying potential 'thick grain boundaries' just below the wetting point in Zn–Al alloys with high zinc content can be instrumental in uncovering evidence of long-range interactions in metal grain boundaries.

Before [88], studies on the GB wetting were limited to scenarios involving metals with a high melting point in contact with metals with a low melting point (typically in the 'big ear' region of the eutectic phase diagram). This often resulted in the observation of convex functions $\theta(T)$ and discontinuities in the derivative $d\theta/dT$ at the transition point T_w, indicative of first-order transitions. The first exploration of wetting grain boundaries in a metal with a low melting point by a liquid phase containing metal atoms with a high melting point (occurring in the 'small ear' region of the eutectic phase diagram) revealed a continuous grain boundary wetting transition (a second-order transition) characterized by a concave function $\theta(T)$ without discontinuities in the derivative $d\theta/dT$ at the point T_w [88]. It is conceivable that continuous phase transitions of GB wetting could be present not only in the 'small ears' of eutectic phase diagrams but also in other locations yet to be explored.

4. Formation of thin layers of grain boundary phases

4.1 Grain boundary solidus in the phase diagram

If in the two-phase region $\alpha + L$ of the phase diagram (see diagrams in Fig. 14 [155]) there is a phase transition from incomplete GB wetting by the melt (Fig. d) in the phase diagram Fig. 14) to complete one (Fig. b), then above the GB wetting tie-line the energy of two interphase boundaries of solid and liquid phases $2\sigma_{SL}$ will be below the energy of the grain boundary σ_{GB}, $2\sigma_{SL} < \sigma_{GB}$. This means that if we replace the grain boundary with a liquid phase interlayer, the system will receive an energy gain equal to $\sigma_{GB} - 2\sigma_{SL}$. Let us now cross the line of bulk solidus and move from the two-phase region (Fig. b) of the phase diagram to the single-phase region (Fig. a), where only a solid solution exists in equilibrium. If we are still close enough to the solidus line (Fig. a), then the energy gain $\sigma_{GB} - 2\sigma_{SL}$ obtained from replacing the grain boundary with melt will allow the system to form a thin melt layer at the grain boundary (see diagram Fig. a). This melt is thermodynamically unstable in volume, but it can exist at the boundary, and the thickness of this layer depends on the magnitude of the energy gain $\sigma_{GB} - 2\sigma_{SL}$. If we are close enough to the solidus line, then such a layer on the GB can actually exist. The further we move away from the line of bulk solidus, the greater the energy loss from the formation of a thermodynamically unstable liquid phase. When the gain becomes equal to the loss, the thin layer of the GB phase will disappear and we will find ourselves in the area (Fig. 14c). At this point on the bulk phase diagram there is a line of grain boundary solidus. Thus, there may be a thin liquid-like layer between the grain boundary and bulk solidus lines at the boundary.

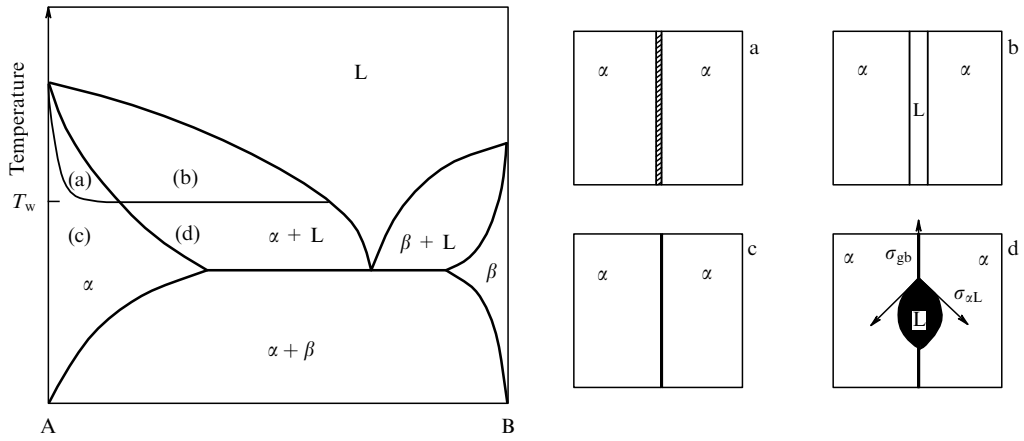

Figure 14. Schematic bulk phase diagram showcasing an additional phase transition tie-line of GB wetting at T_w and its extension in the form of a grain boundary solidus line (the pre-wetting phase transition line at GB). The provided diagrams elucidate the behavior of the solute in the grain boundary (GB) across different regions of the phase diagram: (a) Presence of a liquid-like layer (multilayer adsorption layer) in the single-phase region (solid solution); (b) Complete wetting of the GB by the liquid phase L in the solid phase α within the two-phase region α + L; (c) Typical single-layer segregation on the GB in the single-phase α region; (d) Partial wetting of the GB by the liquid phase L in the α phase within the two-phase α + L region. The illustration has been reprinted from [155] with the permission of the American Physical Society © 2005.

4.2 Grain boundary segregation, electrical conductivity, and faceting between bulk and grain-boundary solidus lines

The presence of such interlayers was investigated in-depth for the first time in the copper–bismuth system [155, 157–163]. It has been well established that even with minimal additions of bismuth to copper, copper polycrystals become significantly embrittled. They can easily break when handled, revealing grain boundaries with a distinct gray color on the fracture surface. This is notable considering that the natural color of pure copper, as commonly known, is reddish-yellow. In essence, all the bismuth, which appears gray, accumulates at the grain boundaries, contributing to increased brittleness of the copper polycrystal with low bismuth content. Hence, a comprehensive investigation into the grain boundary segregation of bismuth was undertaken in the studies [158–161]. The primary focus was on determining the equilibrium solubility of bismuth in copper through experimental means at different temperatures and establishing a solidus line (indicated by the solid line in Fig. 15) [157]. It becomes evident that the equilibrium solubility of bismuth in copper is notably low (not exceeding 200 ppm, equivalent to 2×10^4 at. %), and the solidus line exhibits an atypical s-shape [157].

Subsequently, polycrystals with various bismuth concentrations were fabricated from high-purity copper (99.998 at.%); specifically, 0, 20, 36, 61, 81, 99, 120, 130, and 180 ppm Bi. This was accomplished by situating a pure copper polycrystal within a vacuumed quartz ampoule containing a bismuth vapor source and subjecting it to annealing. An alloy of copper with 2 at.% Bi acted as the source of bismuth vapor, allowing for bismuth diffusion into copper via the gas phase. The quantity of bismuth introduced was reliant on the duration of the annealing process. Subsequently, after ensuring uniform bismuth distribution throughout the sample volume by prolonged annealing of the bismuth-saturated polycrystals, each of the resulting eight alloys underwent annealing at temperatures ranging from 400 to 1050 °C. Following annealing, Auger electron spectroscopy was employed to examine each sample. The process involved fracturing the sample within an Auger spectrometer's sample preparation chamber, followed by extracting a depth concentration profile from the resultant fractured surface. At an initial annealing temperature of 400 °C, all samples exhibited brittleness and experienced grain boundary fracture. Upon examining the exposed surface, identified as the grain boundary, bismuth was observed to form a layer of two monolayers. Although the thickness of the bismuth in two monolayers remained constant initially with increasing pre-

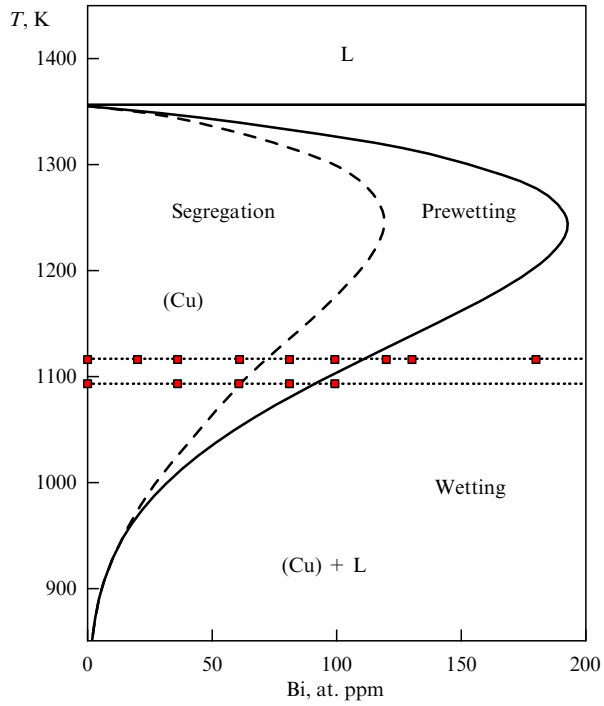

Figure 15. Segment of the copper-rich side of Cu–Bi phase diagram. The solid curve represents a retrograde bulk solidus line [157]. The dashed curve illustrates a grain boundary solidus line determined from Cu–Bi polycrystals [158–161]. The temperatures of diffusion annealing (1116 K and 1093 K) and the bismuth concentrations in the samples are specified (0, 20, 36, 61, 81, 99, 120, 130, and 180 ppm, respectively). L represents the liquid phase; (Cu) denotes a copper-based solid solution. The diagram is adapted from [155] with permission from the American Physical Society © 2005.

annealing temperatures, it abruptly decreased below one monolayer at a specific point and continued to diminish with further temperature increase. Below a bismuth concentration at the grain boundaries that was equivalent to half of a monolayer, the fragility associated with grain boundaries diminished, and the samples resisted fracture along these boundaries. The dashed line in Fig. 15 links the points where the abrupt decline in grain boundary segregation from two monolayers to below one monolayer of bismuth occurred.

Consequently, a bismuth layer measuring a few monolayers in thickness at the grain boundaries was not only observed in the two-phase region (Cu) + L, where the bismuth-containing melt L wets the grain boundaries but also in the single-phase region (Cu), where there is only a solid solution (Cu) in equilibrium within the volume. The authors of [158–161] interpreted this phenomenon as pre-wetting or pre-melting at the boundaries, as predicted by Cahn. Two monolayers of bismuth are present at the grain boundaries to the left of the bulk solidus line but to the right of the grain boundary solidus line. Simultaneously, along the grain boundary solidus line, the bismuth concentration at the boundaries abruptly changes from a multilayer configuration to the standard monolayer segregation.

Subsequently, it was demonstrated that other characteristics of the GBs in copper experience a sudden change at the grain boundary solidus line. For instance, the conductivity of a polycrystal is significantly influenced by the presence of bismuth interlayers in all grain boundaries [161]. In cases where all grain boundaries consist of bismuth layers, high-conductivity copper grains are enclosed by low-conductivity bismuth layers, leading to an overall low conductivity in such a polycrystal. As the pre-annealing temperature is elevated, the proportion of grain boundaries with bismuth gradually diminishes. Eventually, there reaches a point where the continuous network of these boundaries fractures, enabling electrons to navigate along unbroken chains of pure copper grains. Consequently, the conductivity of the sample experiences a remarkable increase [161].

In reference [164], the facetting of twin boundaries in copper alloys with varying bismuth content was examined. It was revealed that at lower bismuth concentrations positioned to the left of the grain boundary solidus (see Fig. 15), the structure and energy of the twin boundaries showed little deviation from those observed in pure copper, as explored previously [40]. When the samples were subjected to annealing within the phase diagram region situated between the bulk and grain boundary solidus, where a thin liquid-like bismuth layer exists at the boundaries, the rate of thermal etching groove formation and its depth experienced a tenfold increase, alongside a noticeable alteration in the equilibrium facets spectrum [164].

4.3 Grain boundary mass transfer between bulk and grain-boundary solidus lines

The rapid growth rate of the thermal etching groove observed at GBs with a liquid-like bismuth layer signifies a high diffusion permeability of these boundaries. In a study [155], the diffusion permeability of GB in Cu–Bi alloys was directly quantified by employing grain-boundary diffusion of radioactive isotopes of bismuth ^{207}Bi and copper ^{64}Cu. Diffusion annealing was conducted at temperatures of 1116 K and 1093 K, with the experimental points' positions illustrated in Fig. 15. Figure 16 shows the relationship between the grain boundary diffusion permeability $P_{\mathrm{Bi}} = s\delta D$ for bismuth and its concentration in Cu–Bi alloys at $T = 1116$ K (a) and 1093 K (b). The symbols indicate the grain boundary segregation coefficient s, the diffusion thickness of the boundary δ, and the grain boundary diffusion coefficient D. The solid and dotted vertical lines correspond to the concentrations of bulk and grain boundary solidus (refer to Fig. 15) [158–161]. Notably, we observe a sharp increase in grain boundary diffusion upon crossing the grain boundary solidus line (by approximately one and a half orders of magnitude), maintaining this elevated level within the phase diagram's two-phase region. Interestingly, the investigated polycrystals feature two categories of grain boundaries. At some of these boundaries, the diffusion permeability experiences a sudden rise upon crossing the GB solidus line (indicated by filled symbols in Fig. 16), whereas at others, it does not (denoted by open symbols). Evidently, the wetting conditions are not met at low-energy boundaries, preventing the formation of bismuth layers. These boundaries remain unobserved in Auger spectroscopy experiments due to the absence of grain boundary fracture along them.

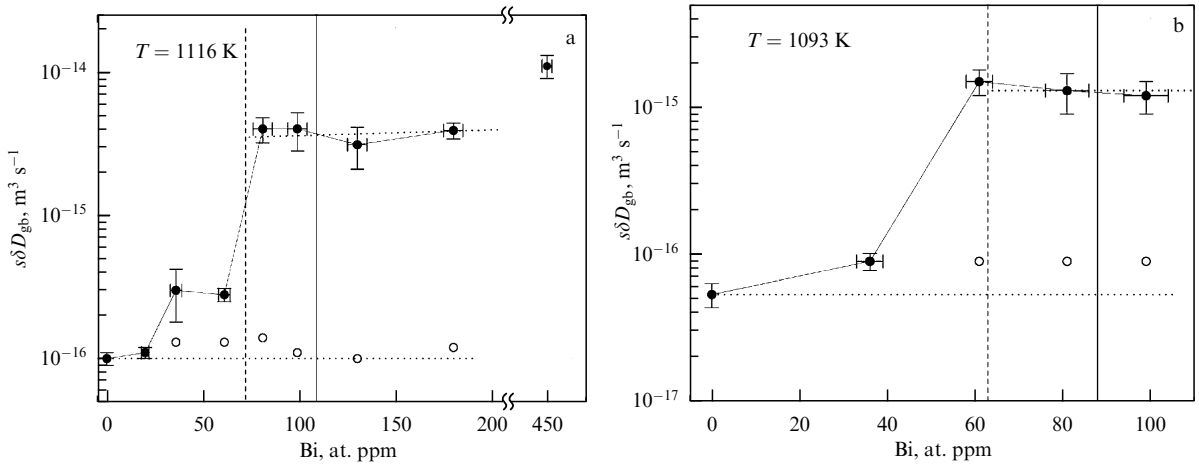

Figure 16. The relationship between GB diffusion permeability for bismuth P_{Bi} and concentration in Cu–Bi alloys at $T = 1116$ K (a) and 1093 K (b) is depicted. The filled and open symbols correspond to the P_{fast} and P_{slow} values respectively. The solid and dotted vertical lines represent the concentration of bulk and grain-boundary solidus respectively [158–161]. Meanwhile, the dotted horizontal lines signify the diffusion permeability for bismuth in pure copper and in two-phase Cu–Bi alloys. This illustration has been reproduced from [155] with the permission of the American Physical Society © 2005.

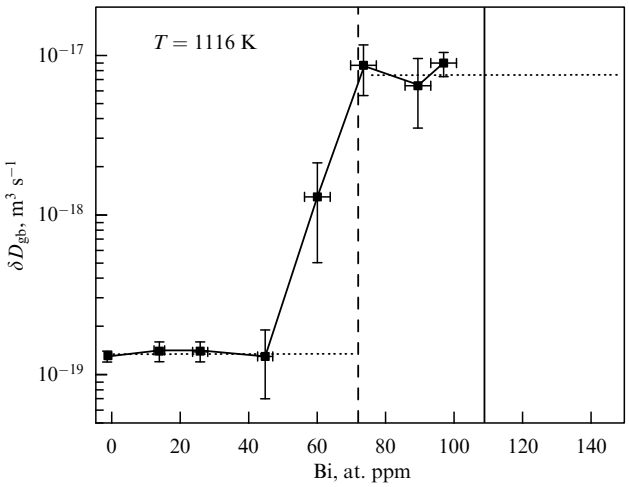

Figure 17. Dependence of GB diffusion permeability for copper P_{Cu} and concentration in Cu–Bi alloys at a temperature of $T = 1116$ K. The dotted lines in the figure denote the diffusion permeability for copper in solid solution and in two-phase Cu–Bi alloys. This diagram has been reproduced from [155] with the permission of the American Physical Society © 2005.

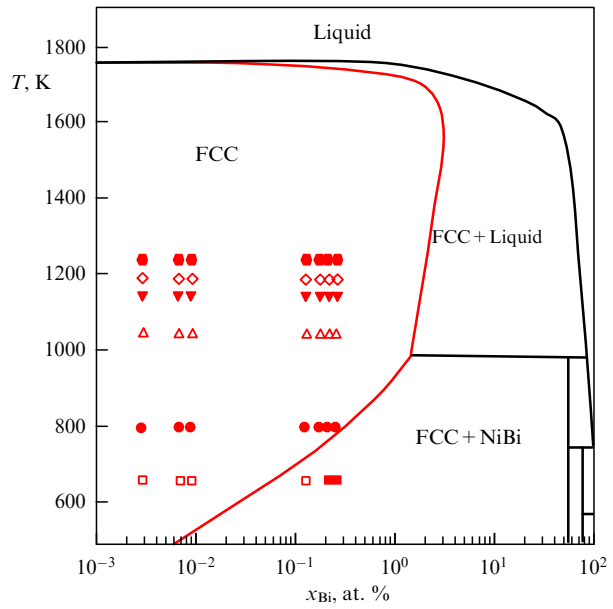

Figure 18. Ni–Bi phase diagram. The red symbols indicate the experimental conditions for measuring the tracer diffusion. The drawing is reprinted from [165] with permission from Elsevier © 2023.

The diffusion permeability for atoms of the copper tracer ^{64}Cu exhibits a similar pattern (Fig. 17). To the left of the grain boundary solidus, the diffusion permeability of copper is low at low bismuth concentrations. Upon reaching the dotted line marking the grain boundary solidus, it escalates by roughly two orders of magnitude and retains a high level between the grain-boundary and bulk solidus lines, where a liquid-like phase is present at the boundary.

Liquid-like thin layers were observed at GBs in the single-phase region of the Ni–Bi system, where only a solid solution exists in equilibrium in the volume. This behavior is similar to what is seen in the Cu–Bi system (refer to Fig. 18) [165]. In contrast to the Cu–Bi system, the solubility of bismuth in nickel is significantly higher, reaching up to 1 at.% Bi. Consequently, the authors of [165] managed to map numerous experimental points in the single-phase region and identify transitions between grain-boundary layers of bismuth varying in thickness (Fig. 19).

The left column in Fig. 19 displays EBSD images of nickel alloys with varying bismuth contents: Ni–0.14 at.% Bi (a), Ni–0.21 at.% Bi (b), Ni–0.23 at.% Bi (c), and Ni–0.28 at.% Bi (d). Through EBSD analysis depicted in the left column of Fig. 19, it was observed that all samples exhibit a random texture. This uniformity enables a reliable comparison of GB diffusion properties across samples with differing bismuth concentrations. Figures 19a–p present examples of micrographs in HAADF-STEM mode, corresponding EDS concentration maps, and selected results of linear scanning of grain boundaries, all essential for analyzing the tracer diffusion. HAADF-STEM images confirm bismuth segregation on the grain boundaries in Ni–Bi alloys annealed at 1123 K (refer to Fig. 18). It is evident that the thickness of the bismuth segregation layer at the grain boundary increases as the bismuth concentration in the alloy rises, indicating movement within the single-phase region towards the bulk solidus.

Figure 20 depicts the concentration dependencies of the GB diffusion permeability P_{Bi} for the nickel tracer ^{63}Ni in Ni–Bi alloys at five different temperatures. The graph features blue and yellow dotted lines representing three concentration regions exhibiting distinct diffusion permeability behaviors. In region I, the diffusion permeability of the boundaries in nickel-bismuth alloys remains consistent with the values for pure nickel. Notably, the recorded diffusion permeability values for the nickel isotope using GB in pure nickel align with the contribution of random high-angle GB of a general type, matching the highest diffusion rates observed in a well-annealed polycrystalline material [166, 167]. Upon the addition of bismuth to nickel, the diffusion permeability values consistently rise.

As shown in the image TEM in inset, the grain boundaries in nickel in region I do not exhibit bismuth-rich interlayers. The bismuth enrichment at the boundaries is limited to a typical single-layer segregation. In region II, situated between the blue and yellow dotted lines, there is a significant increase in the diffusion permeability of the boundaries by approximately two orders of magnitude. Concurrently, bismuth-rich layers start to appear at GBs (refer to the inset). Moving to region III to the right of the yellow dotted line, the high diffusion permeability remains relatively constant, with all boundaries hosting liquid-like layers of bismuth (as depicted in the inset). The stability of the diffusion permeability in region III is clearly evident in Fig. 21, illustrating the concentration dependence of the GB diffusion permeability at a temperature of 650 K. In this scenario, regions I and II are relatively narrow, leaving predominantly a (albeit quite broad) region III.

The bismuth-rich interlayers can exhibit varying thicknesses at the same boundary. This variability is clearly evident on the EDS grain boundary map in the Ni–0.28 at.% Bi alloy annealed at 650 K (Fig. 22b). Linear scan 1 intersects the boundary where bismuth is nearly undetectable (Fig. 22c). On the other hand, linear scan 2 intersects the grain boundary at a point where the interlayer thickness measures approximately 5–10 nm (Fig. 22d). This observation suggests the presence of diverse high-angle crystals in the analyzed polycrystals, showing varying degrees of bismuth segregation, ranging from ‘pure’ to bismuth-enriched.

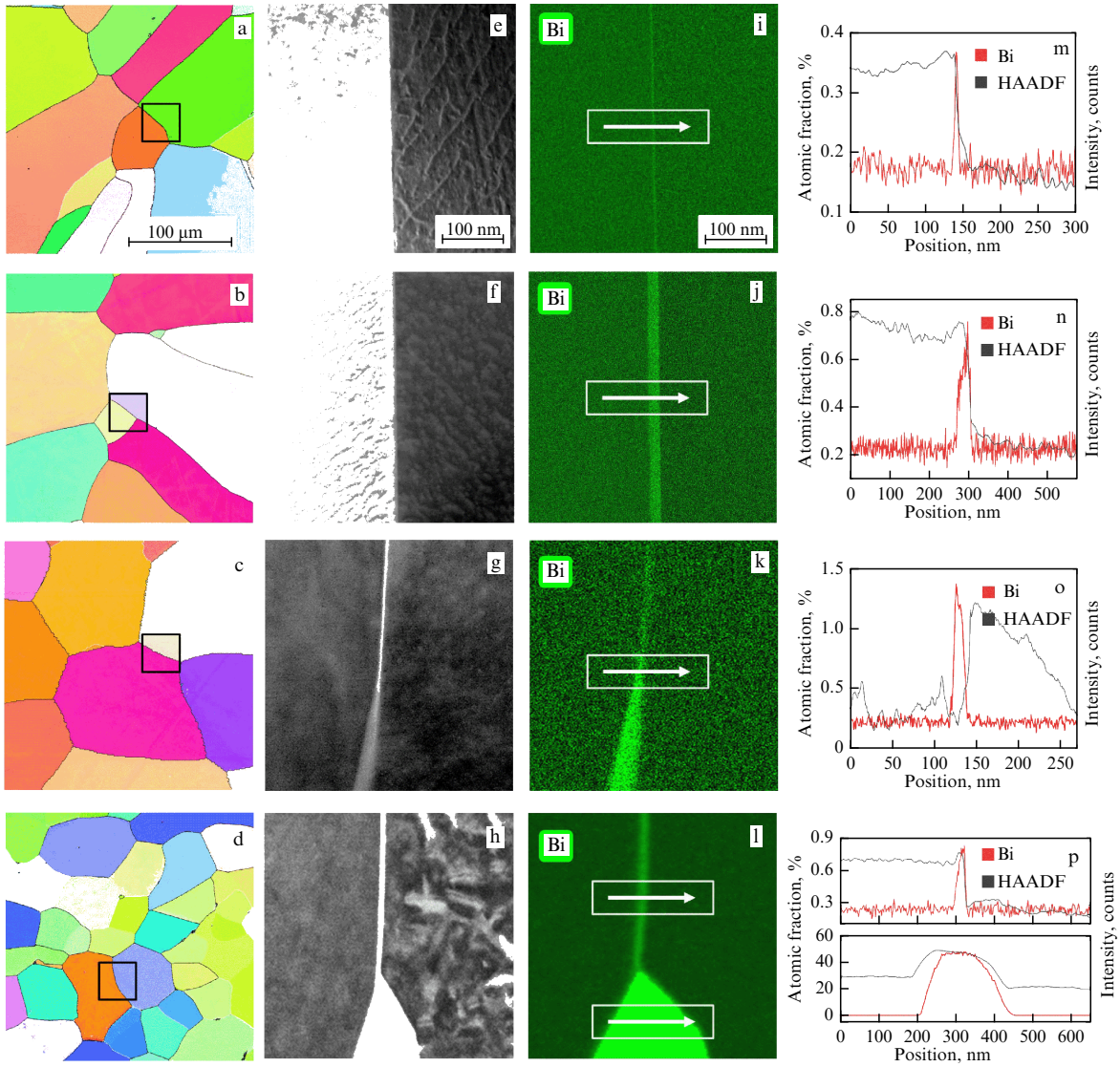

Figure 19. TEM images of nickel alloys with varying bismuth contents: (a) Ni–0.14 at.% Bi, (b) Ni–0.21 at.% Bi, (c) Ni–0.23 at.% Bi, and (d) Ni–0.28 at.% Bi, focusing on the grain boundaries. The left column (a, b, c, d) displays the EBSD images. The second column (e, f, g, h) showcases HAADF-STEM images. The subsequent column (i, j, k, l) exhibits the corresponding EDS maps for bismuth, while the rightmost column (m, n, o, p) presents the results of linear scanning along the lines depicted in the micrographs (i, j, k, l). The scales provided for a nickel alloy with a bismuth content of 0.14 at.% Bi apply to images (f, g, h) and (j, k, l) accordingly. Grain boundaries displaying layers of bismuth with varying thicknesses are clearly discernible. This diagram is reproduced from [165] with permission from the Elsevier © 2023.

Consequently, this diversity may account for the existence of two distinct diffusion coefficients as depicted in Fig. 21.

The heterogeneity of the bismuth-rich layers was verified through atomic probe tomography (APT) examinations. In Fig. 23, the results of APT measurements for Ni–0.28 at.% Bi alloy are depicted. Areas exhibiting high-angle grain boundaries enriched in bismuth were chosen for sample preparation in APT. Figure 22 (central panel) displays a TEM micrograph and an accurate reconstruction image portraying one side of the grain boundary with a bismuth-enriched particle. This observation confirms the significant variation in bismuth distribution throughout the sample under scrutiny. The bismuth concentration within the particle reaches approximately 90 at.% as illustrated in the histogram found in the right panel of Fig. 23. The thickness of the bismuth-enriched layer in this region measures about 10 nm.

The experimental data presented reveal a series of grain boundary phase transitions induced by bismuth within the single-phase Ni(Bi) solid solution region on the bulk phase diagram. This scenario differs significantly from that observed in Cu–Bi alloys, where a distinct and sudden increase in diffusion rates along the grain boundary was linked to a pre-melting grain boundary phase transition [158–161]. In the context of Ni–Bi alloys, the diffusion coefficients in accordance with the Gruzinov–Zavaritsky (GZ) model show a systematic increase with higher bismuth concentrations. Notably, at elevated temperatures in region III, the triple product values of nickel diffusion coefficients following the GZ model, given by $P = s\delta D_{gb}$, are approximately 10^{-18} m^3 s^{-1}, as depicted in Fig. 7. Assuming limited nickel segregation on the grain boundaries in these alloys and a GB thickness (δ) of around 1 nm, these triple product values of P correspond to diffusion coefficients for grain boundaries

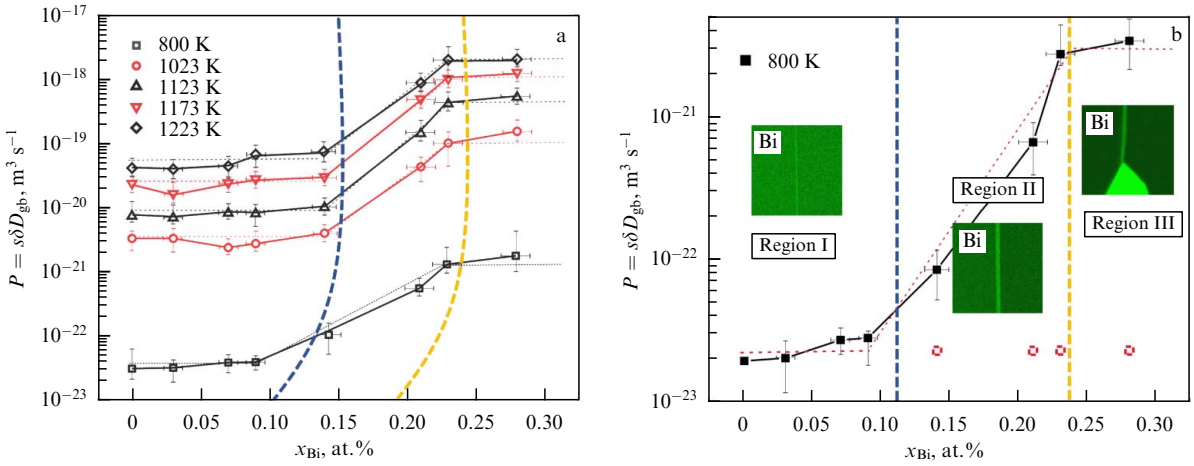

Figure 20. Concentration dependencies of the GB diffusion permeability P_{Bi} for the diffusion of the nickel tracer ^{63}Ni in Ni–Bi alloys at five different temperatures (a). In Fig. b, an enlarged view of the data measured at $T = 800$ K is provided, with the red open circles indicating the diffusion coefficient for pure nickel. The graph outlines three distinct regions with varying concentration dependencies of the diffusion permeability of the boundaries. The insets showcase corresponding EDS maps for bismuth in three different Ni–Bi alloys. This illustration is reproduced from [165] with permission from Elsevier © 2023.

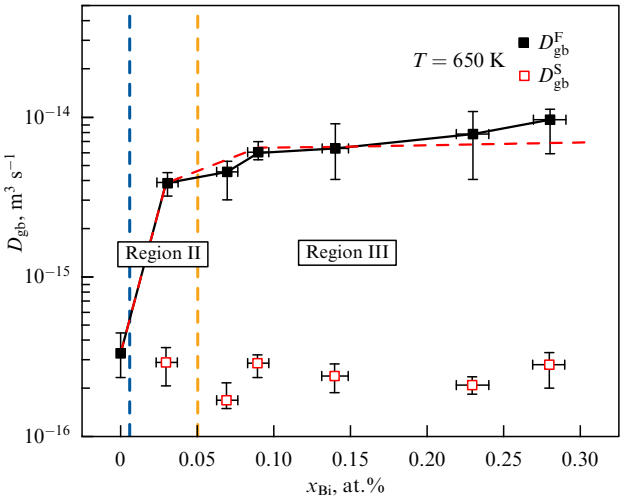

Figure 21. The concentration dependency of the diffusion permeability P_{Bi} of the Ni–Bi boundaries for the diffusion of the nickel tracer ^{63}Ni in Ni–Bi alloys at $T = 650$ K is illustrated. Solid black symbols represent rapid diffusion along the GB, while open red circles indicate slow diffusion along the GB. The diagram is reproduced from [165] with permission from Elsevier © 2023.

(D_{gb}) on the order of 10^{-9} m^2 s^{-1}, typical of diffusion in molten materials.

Furthermore, it has been observed that the triple product values measured for compositions falling within region III are nearly consistent, with differences falling within the usual range of experimental error. This outcome is somewhat unexpected, as one would anticipate an increase in the diffusion coefficient. It is hypothesized that the presence of wetting/pre-wetting interlayers may lead to significantly high diffusion coefficients in all compositions falling under region III. Therefore, the data collected enables to infer the presence of a grain-boundary wetting/pre-wetting phase transition in the Ni–Bi system (region III) and, as a result, the presence of a liquid-like layer on the grain boundary between the lines of the bulk and grain-boundary solidus in this system (Fig. 24).

The process of 'activated sintering' is known to harness increased grain-boundary diffusion facilitated by the presence of wetting/pre-wetting layers on the GB [168, 169]. Classical theories on grain boundary phases acknowledge the existence of three distinct types of GB: (1) pure GB, (2) single-layer Langmuir–McLean (L–M) segregation, and (3) multi-layer GB featuring a wetting/pre-wetting film [170]. When adopting the language of grain boundary complexions and transitions between them, two-layer and multi-layer complexions are differentiated [171]. Transmission electron microscopy (TEM) micrographs obtained through high-resolution transmission electron microscopy (HRTEM) on Ni–Bi alloys annealed at 1123 K revealed four distinct phases on the GB (Fig. 25): (a) classical single-layer L–M bismuth adsorption in Ni alloy with 0.14 at.% Bi, (b) two-layer and three-layer adsorption in Ni alloy with 0.21 at.% Bi, (c) multilayer adsorption in Ni alloy with 0.23 at.% Bi, and (d) the intercrystalline film in Ni alloy with 0.28 at.% Bi. In [165], investigations were conducted on at least two different grain boundaries in each alloy, revealing a full correspondence to the GB phases previously described for Ni–Bi alloys [170, 172, 173]. Moreover, in [165], a sequential transition between different phases on the GB was showcased for the first time, closely tied to variations in GB diffusion rates. Additionally, the segregation of bismuth in the Ni alloy with 0.21 at.% Bi was found to be heterogeneous, with transitions occurring between two- and three-layer adsorptions along the same interface (refer to Fig. 25e).

The standard Ni–Bi bulk phase diagram fails to account for the series of grain boundary phase transformations observed in diffusion experiments. As a result, a grain boundary phase diagram was constructed in [165] to elucidate the identified GB transitions in the Ni–Bi system (refer to Fig. 26). The two dashed curves denote the shift between 'pure' GB and GB enriched with a layer of bismuth (indicated by the blue dashed line) and the grain boundary solidus (highlighted by the yellow dashed line). The red line represents the bulk solidus, while the orange dashed line signifies the grain boundary transition line of the first order, as theorized by Zhou et al. [174]. The diagrams on the left and

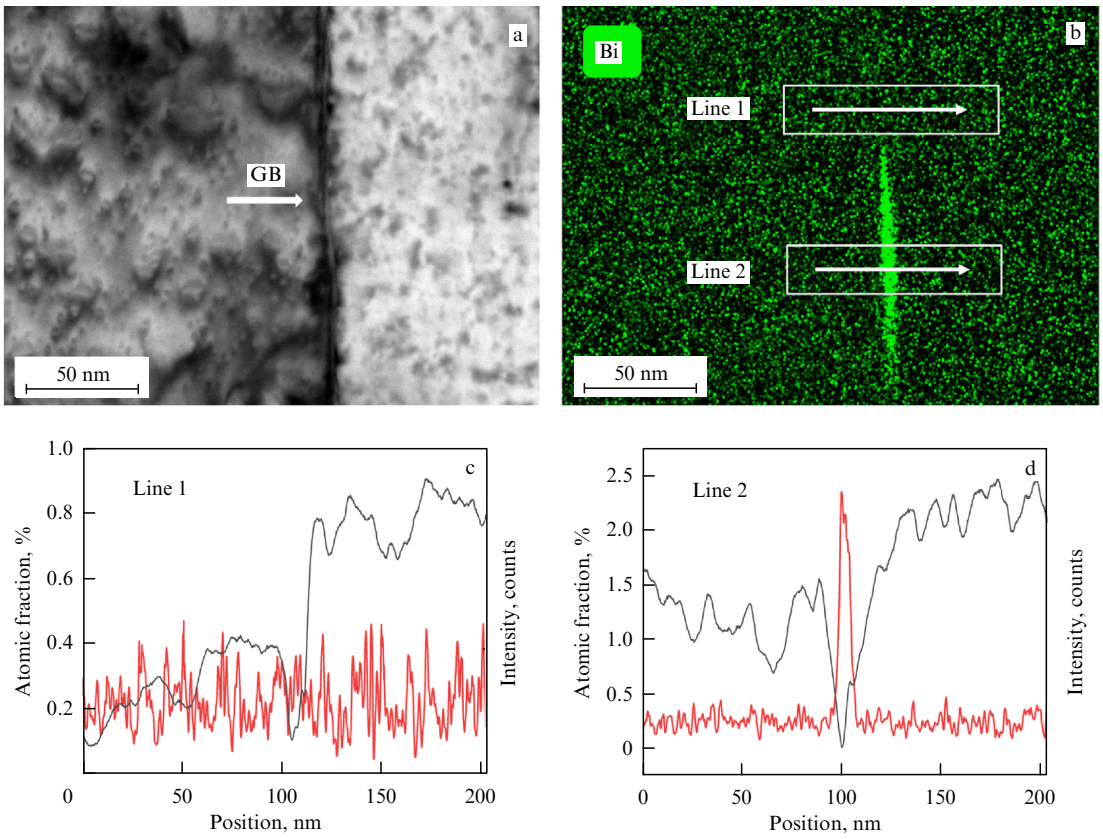

Figure 22. HAADF image of the Ni–0.28 at.% Bi alloy annealed at 650 K (a), accompanied by the EDS maps for bismuth (b) and the outcomes of two specific linear scans (c, d). The paths of the linear scans are delineated in Fig. b. The diagram is reprinted from [165] with permission from Elsevier © 2023.

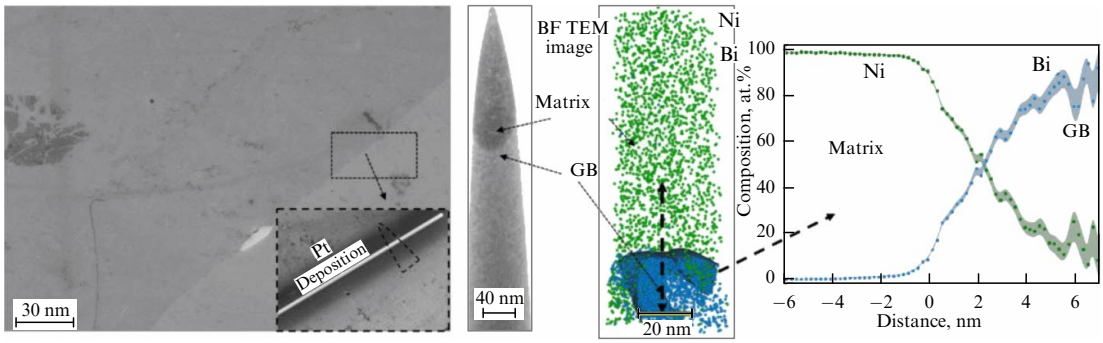

Figure 23. Examination of bismuth segregation via atomic probe tomography (APT) in Ni–0.28 at.% Bi alloy: Scanning Electron Microscope (SEM) image captured with a high-angle lens (left panel), Transmission Electron Microscope (TEM) image of the tip and its APT reconstruction (central panel), and concentration histogram (right panel). The illustration has been reprinted from [165] with the permission of Elsevier © 2023.

right showcase the structures of grain boundary complexions corresponding to the specific regions of the grain boundary phase diagram.

5. Conclusions

1. Within grain boundaries (intercrystalline boundaries), solid materials can undergo various phase transformations, similar to bulk ones.

2. Primarily, these transformations involve faceting–roughening. The facets on the grain boundary represent planes that align with the densely packed planes of the superlattice shared by the two adjoining grains (coincidence sites lattice — CSL). With increasing temperature, these facets may vanish, giving way to an rounded GB as a consequence of a first- or second-order transition. Conversely, as temperature decreases, equilibrium GB facets emerge with higher CSL indices.

3. The grain boundary can be wetted by additional layers of a second phase, whether liquid or solid. This wetting can either be complete, where the second phase entirely substitutes the grain boundary, or incomplete (partial), manifesting as a chain of droplets or solid particles on the grain boundary. Transitions between complete and incomplete wetting can occur as first or second order (continuous) transitions.

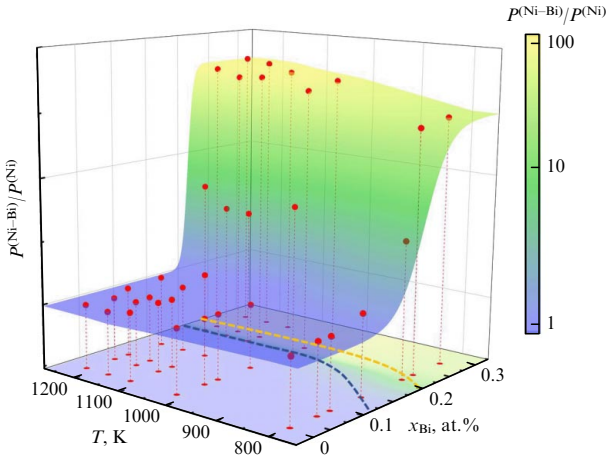

Figure 24. Three-dimensional graph illustrating the dependence of the ratio P(Ni–Bi)/PNi of nickel diffusion coefficients in the Gruzinov–Zavaritsky (GZ) model on concentration for Ni–Bi alloys. The solid symbols on the graph correspond to the experimental values of the triple product *P*. The purple region signifies zone I, known as the 'clean GB zone,' while the green region represents zone II, indicating the transition area for GB. Lastly, the yellow region denotes zone III, which represents the wetting/pre-wetting phase area on the GB. This illustration has been adapted from [165] with permission from Elsevier © 2023.

4. Thin layers of the grain boundary phase may develop on the grain boundary, remaining stable at the interface while being unstable in the bulk. Such phenomena result from pre-wetting, pre-melting, or pseudo-incomplete wetting phase transformations.

5. Phase transformations within the grain boundary significantly impact the properties of the polycrystal as a whole, leading to the emergence of new grain boundary lines in the bulk phase diagrams.

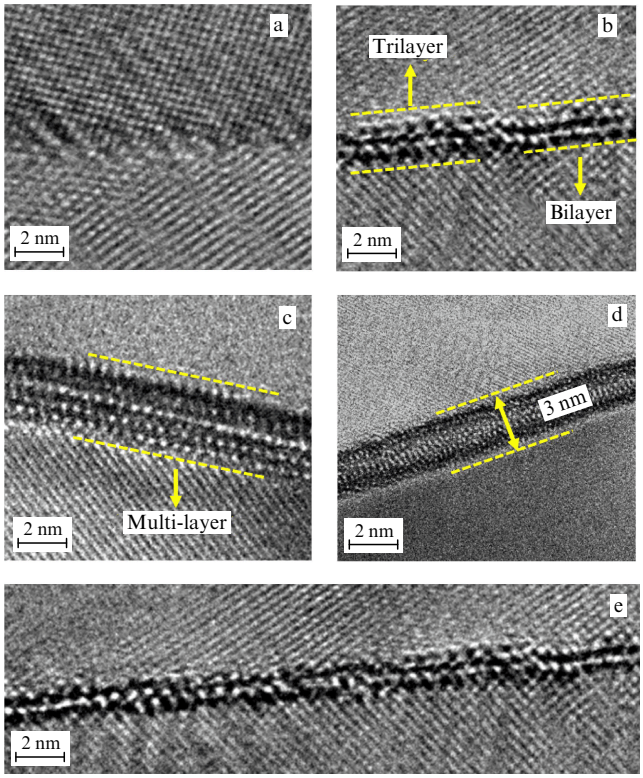

Figure 25. Examples of phases observed at the grain boundaries in alloys containing Ni–0.14 at.% Bi (a), Ni–0.21 at.% Bi (b), Ni–0.23 at.% Bi (c), and Ni–0.28 at.% Bi (d) after annealing at 1123 K. As the bismuth content in Ni–Bi alloys increases, a series of transitions are observed from (a) traditional monolayer adsorption on GB to (b) two- and three-layer adsorption, (c) multilayer adsorption, and ultimately to (d) a liquid-like film. Simultaneously, in the Ni–0.21 at.% Bi alloy (e), a distinctive shift between two-layer and three-layer segregation along the same GB was identified. The diagram has been reproduced from [165] with permission from Elsevier © 2023.

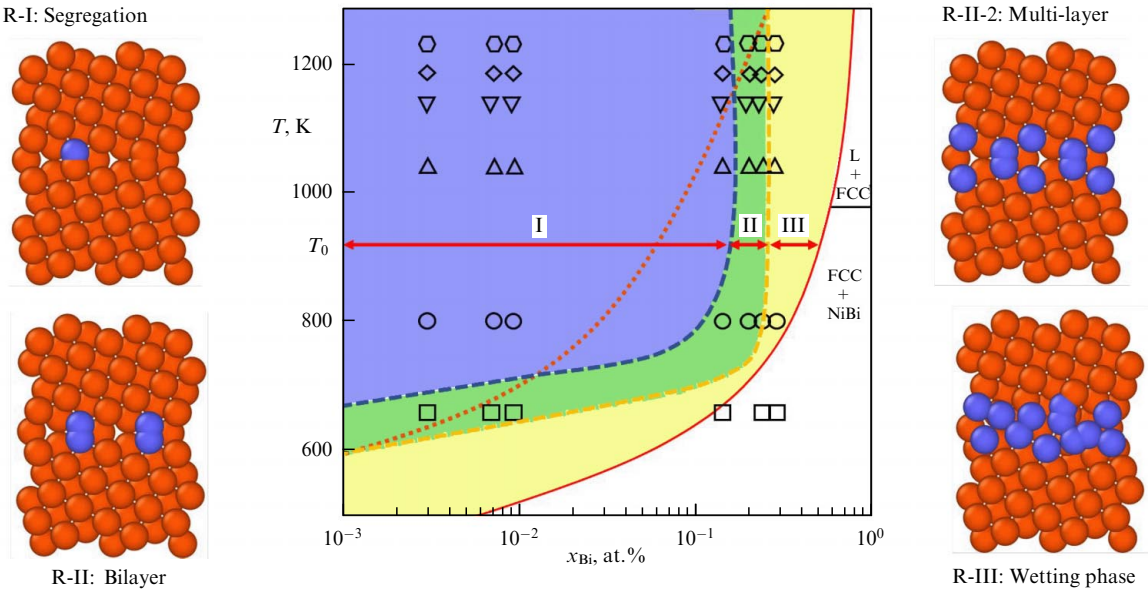

Figure 26. Schematic GB phase diagram for the Ni–Bi system. The two dashed lines represent the transition between 'pure' GB and GB enriched with a layer of bismuth (indicated by the blue dashed line) and the grain boundary solidus (highlighted by the yellow dashed line). The red line denotes the bulk solidus, while the orange dashed line indicates the grain boundary transition line of the first order as hypothesized by Zhou et al. [174]. The diagrams on the left and right illustrate the structures of grain boundary complexions corresponding to specific zones within the grain boundary phase diagram. This diagram is reproduced from [165] with permission from Elsevier © 2023.

References

1. Gibbs J W *Trans. Connecticut Acad. Arts Sci.* **3** 343 (1878)
2. Gibbs J W *On the Equilibrium of Heterogeneous Substances* (New York: Longmans, Green and Co, 1928)
3. Hoffman D W, Cahn J W *Surf. Sci.* **31** 368 (1972)
4. Cahn J W, Hoffman D W *Acta Metall.* **22** 1205 (1974)
5. Curie P *Bull. Soc. Min. France* **8** 145 (1885)
6. Wulff G V *Trudy Obshchestva Estestvoisp. pri Imperator. Varshavsk. Univ.* **6** (9) 7 (1894–1895)
7. Wulff G *Z. Kristallogr.* **34** 449 (1901)
8. Landau L D *Sobranie Trudov* (Collected Works) Vol. 2 (Moscow: Nauka, 1969) p. 119–125; in *Sbornik, Posvyashchennyi Semidesyatiletiyu Akademika A.F. Ioffe* (Collection Honoring the 70th Anniversary of the Birth of Academician A.F. Ioffe) (Moscow: Izd. AN SSSR, 1950) p. 44
9. Burton W K, Cabrera N *Disc. Faraday Soc.* **5** 33 (1949)
10. Burton W K, Cabrera N, Frank F C *Philos. Trans. R. Soc. London A* **243** 299 (1951)
11. Chernov A A *Sov. Phys. Usp.* **4** 116 (1961); *Usp. Fiz. Nauk* **73** 277 (1961)
12. Lee S B, Han H N *Sci. Rep.* **11** 15563 (2021)
13. Marchenko V I *Sov. Phys. JETP* **54** 605 (1981); *Zh. Eksp. Teor. Fiz.* **81** 1141 (1981)
14. Landa A et al. *J. Non-Cryst. Solids* **205–207** 767 (1996)
15. Gravil P A, Holloway S *Phys. Rev. B* **53** 11128 (1996)
16. Heyraud J C, Mėtois J J *J. Cryst. Growth* **84** 503 (1987)
17. Heyraud J C, Mėtois J J *J. Cryst. Growth* **50** 571 (1980)
18. Heyraud J C, Mėtois J J *J. Cryst. Growth* **98** 355 (1989)
19. Rottman C, Wortis R *Phys. Rev. B* **29** 328 (1984)
20. Wagner R et al. *Phys. Rev. Lett.* **76** 263 (1996)
21. Fradkov V E, Shvindlerman L S *Poverkhnost'. Fiz., Khim., Mekh.* (11) 50 (1982)
22. Kosevich V M, Baizul'din B M *Fiz. Med. Metalloved.* **48** (2) 442 (1979)
23. Muschik T et al. *Z. Metallkd.* **84** 596 (1993)
24. Muschik T et al. *Acta Metall. Mater.* **41** 2163 (1993)
25. Barg A, Rabkin E, Gust W *Acta Metall. Mater.* **43** 4067 (1995)
26. Krakow W, Smith D A *Ultramicroscopy* **22** 47 (1987)
27. Hsieh T E, Balluffi R W *Acta Metall.* **37** 2133 (1989)
28. Prokofjev S I *Defect Diffusion Forum* **194–199** 1141 (2001)
29. Ratanaphan S et al. *Acta Mater.* **88** 346 (2015)
30. Schuh C A, Kumar M, King E *J. Mater. Sci.* **40** 847 (2005)
31. Jin Y et al. *J. Mater. Sci.* **50** 5191 (2015)
32. Randle V et al. *Acta Mater.* **56** 2363 (2008)
33. Olmsted D L, Foiles S M, Holm E A *Acta Mater.* **57** 3694 (2009)
34. Beladi H, Rohrer G S *Acta Mater.* **61** 1404 (2013)
35. Beladi H, Rohrer G *Metall. Mater. Trans. A* **44** 115 (2013)
36. Glowinski K, Morawiec A *J. Mater. Sci.* **49** 3936 (2014)
37. Ratanaphan S, Yoon Y, Rohrer G S *J. Mater. Sci.* **49** 4938 (2014)
38. Straumal B B et al. *Interface Science* **9** 287 (2001)
39. Straumal B B, Shvindlerman L S *Acta Metall.* **33** 1735 (1985)
40. Straumal B B, Polyakov S A, Mittemeijer E J *Acta Mater.* **54** 167 (2006)
41. Taylor J E, Cahn J W, Handwerker C A *Acta Metall. Mater.* **40** 1443 (1992)
42. Cahn J W, Carter W C *Metall. Mater. Trans. A* **27** 1431 (1996)
43. Maksimova E L, Shvindlerman L S, Straumal B B *Acta Metall.* **36** 1573 (1988)
44. Wolf U et al. *Philos. Mag. A* **66** 991 (1992)
45. Ernst F et al. *Z. Metallkd.* **87** 911 (1996)
46. Forwood C T, Clarebrough L M *Acta Metall.* **32** 757 (1984)
47. Clarebrough L M, Forwood C T *Phys. Status Solidi A* **60** 51 (1980)
48. Merkle K L, Wolf D *Philos. Mag. A* **65** 523 (1992)
49. Goodhew P J, Tan T Y, Balluffi R W *Acta Metall.* **26** 557 (1978)
50. Ernst F et al. *Z. Metallkd.* **87** 911 (1996)
51. Wolf U et al. *Philos. Mag. A* **66** 991 (1992)
52. Ernst F et al. *Phys. Rev. Lett.* **69** 620 (1992)
53. Hofmann D, Finnis M W *Acta Metall. Mater.* **42** 3555 (1994)
54. Brown J A, Mishin Y *Phys. Rev. B* **76** 134118 (2007)
55. Keshishev K O, Parshin A Ya, Babkin A V *Sov. Phys. JETP* **53** 362 (1981); *Zh. Eksp. Teor. Fiz.* **80** 716 (1981)
56. Heyraud J C, Metois J J *Acta Metal.* **28** 1789 (1980)
57. Heyraud J C, Metois J J *Surf. Sci.* **128** 334 (1983)
58. Fisher D S, Weeks J D *Phys. Rev. Lett.* **50** 1077 (1983)
59. Nozieres P, Gallet F *J. Physique* **48** 353 (1987)
60. Berezinskii V L *Sov. Phys. JETP* **32** 493 (1971); *Zh. Eksp. Teor. Fiz.* **59** 907 (1971)
61. Berezinskii V L *Sov. Phys. JETP* **34** 610 (1972); *Zh. Eksp. Teor. Fiz.* **61** 1144 (1971)
62. Kosterlitz J M, Thouless D J *J. Phys. C* **6** 1181 (1973)
63. Grimmer H, Bollmann W, Warrington D T *Acta Cryst. A* **30** 197 (1974)
64. Rybin V V, Perevezentsev V N *Sov. Phys. Solid State* **17** 2103 (1975); *Fiz. Tverd. Tela* **17** 3188 (1975)
65. Gallagher P C J *Metall. Trans.* **1** 2429 (1970)
66. Murr L E *Interfacial Phenomena in Metals and Alloys* (Reading, MA: Addison-Wesley Publ. Co., 1975)
67. Pokrovsky V L, Talapov A L *Phys. Rev. Lett.* **42** 65 (1979)
68. Andreev A F *Sov. Phys. JETP* **53** 1063 (1981); *Zh. Eksp. Teor. Fiz.* **80** 2042 (1981)
69. Wolf P E, Balibar S, Gallet F *Phys. Rev. Lett.* **51** 1366 (1983)
70. Kogtenkova O et al. *Z. Metallkd.* **96** 216 (2005)
71. Protasova S G, Kogtenkova O A, Straumal B B *Mater. Sci. Forum* **558** 949 (2007)
72. Straumal B B et al. *Z. Metallkd.* **96** 161 (2005)
73. Straumal B B et al. *Phys. Rev. Lett.* **92** 196101 (2004)
74. Straumal B B et al. *J. Mater. Sci.* **40** 871 (2005)
75. Arenhold K et al. *Surf. Sci.* **417** L1160 (1998)
76. Straumal B, Sursaeva V, Baretzky B *Scr. Mater.* **62** 924 (2010)
77. Bruggeman G A, Bishop G H, Hartt W H, in *The Nature and Behavior of Grain Boundaries. A Symp. TMS-AIME Fall Meeting in Detroit, Michigan, October 18–19, 1971* (Ed. H Hu) (New York: Plenum Press, 1972) p. 83, DOI:10.1007/978-1-4757-0181-4_4
78. Sursaeva V G et al. *Acta Mater.* **56** 2728 (2008)
79. Rottman C, Wortis M *Phys. Rev. B* **24** 6274 (1981)
80. Straumal B B, Gornakova A S, Sursaeva V G *Crystallogr. Rep.* **54** 1070 (2009); *Kristallogr.* **54** 1123 (2009)
81. Nakhodkin N, Kulish N, Rodionova T *Phys. Status Solidi A* **207** 316 (2010)
82. Nakhodkin N, Kulish N, Rodionova T *J. Cryst. Growth* **381** 65 (2013)
83. Chen J et al. *Superlatt. Miscrostruct.* **36** 369 (2004)
84. Kim Y-J et al. *JOM* **66** 2288 (2014)
85. Kumar A K N, Watabe M, Kurokawa K *Vacuum* **88** 88 (2013)
86. Yoshino T et al. *Contrib. Mineral. Petrol.* **152** 169 (2006)
87. Straumal B, Gust W, Molodov D *Interface Science* **3** 127 (1995)
88. Straumal B B et al. *Phys. Rev. B* **78** 054202 (2008)
89. Schölhammer J et al. *Interface Science* **9** 43 (2001)
90. Straumal B B et al. *J. Mater. Sci.* **45** 2057 (2010)
91. López G A, Mittemeijer E J, Straumal B B *Acta Mater.* **52** 4537 (2004)
92. Straumal B B et al. *JETP Lett.* **100** 535 (2014); *Pis'ma Zh. Eksp. Teor. Fiz.* **100** 596 (2014)
93. Straumal B B et al. *Materials* **14** 7506 (2021)
94. Cahn J W *J. Chem. Phys.* **66** 3667 (1977)
95. Ebner C, Saam W F *Phys. Rev. Lett.* **38** 1486 (1977)
96. de Gennes P G *Rev. Mod. Phys.* **57** 827 (1985)
97. Sullivan D E, Telo da Gama M M, in *Fluid Interfacial Phenomena* (Ed. C A Croxton) (New York: Wiley, 1986)
98. Dietrich S, in *Phase Transitions and Critical Phenomena* Vol. 12 (Eds C Domb, J L Lebowitz) (London: Academic Press, 1988)
99. Schick M, in *Liquids at Interfaces* (Les Houches Summer School Lectures, Session XLVIII, 1988, Eds J Charvolin et al.) (Amsterdam: Elsevier, 1990)
100. Bonn D, Ross D *Rep. Prog. Phys.* **64** 1085 (2001)
101. Passerone A, Eustathopoulos N, Desré P *J. Less-Common Met.* **52** 37 (1977)
102. Passerone A, Sangiorgi R, Eustathopoulos N *Scripta Metall.* **16** 547 (1982)
103. Eustathopoulos N *Int. Metals Rev.* **28** 189 (1983)
104. Straumal B B *Fazovye Perekhody na Granitsakh Zeren* (Phase Transitions at Grain Boundaries) (Moscow: Nauka, 2003)
105. Straumal B et al. et al. *Acta Metall. Mater.* **40** 939 (1992)
106. Straumal B, Molodov D, Gust W *Interface Science* **3** 127 (1995)

107. Straumal B, Gust W, Watanabe T *Mater. Sci. Forum* **294–296** 411 (1999)
108. Noskovich O I et al. *Acta Metall. Mater.* **39** 3091 (1991)
109. Straumal B B et al. *Acta Metall. Mater.* **40** 795 (1992)
110. Chang L-S et al. *Acta Mater.* **47** 4041 (1999)
111. Straumal B et al., in *Nanomaterials by Severe Plastic Deformation. Proc. of the Conf. Nanomaterials by Severe Plastic Deformation, NANOSPD2, December 9–13, 2002, Vienna, Austria* (Eds M J Zehetbauer, R Z Valiev) (Weinheim: Wiley–VCH, 2004)
112. Pezzotti G, Nakahira A, Tajika M *J. Eur. Ceram. Soc.* **20** 1319 (2000)
113. Furukawa Y et al. *J. Ceram. Soc. Jpn.* **104** 900 (1996)
114. Elfwing M, Osterlund R, Olsson E *J. Am. Ceram. Soc.* **83** 2311 (2000)
115. Wang H, Chiang Y-M *J. Am. Ceram. Soc.* **81** 89 (1998)
116. Tanaka I et al. *J. Am. Ceram. Soc.* **77** 911 (1994)
117. Molodov D A et al. *Philos. Mag. Lett.* **72** 361 (1995)
118. Straumal B et al. *Crystals* **13** 1538 (2023)
119. Protasova S G et al. *J. Mater. Sci.* **49** 4490 (2014)
120. Straumal B B et al. *Phys. Met. Metallogr.* **113** 1244 (2012)
121. Straumal B B et al. *Phys. Status Solidi B* **248** 581 (2011)
122. Straumal B B, Sluchanko N E, Gust W *Defect Diffusion Forum* **188-190** 185 (2001)
123. Islam S H, Qu X, He X *Powder Metal.* **50** 11 (2007)
124. Wei D Q, Meng Q C, Jia D C *Ceram. Int.* **33** 221 (2007)
125. Solek K P, Kuziak R M, Karbowniczek M *Arch. Metall. Mater.* **52** 25 (2007)
126. Ji Z S, Hu M L, Zheng X P *J. Mater. Sci. Technol.* **23** 247 (2007)
127. Shatilla Y A, Loewen E P *Nucl. Technol.* **151** 239 (2005)
128. Dietrich S, Schick M *Phys. Rev. B* **31** 4718 (1985)
129. Saam W F, Shenoy V B *J. Low Temp. Phys.* **101** 225 (1995)
130. Shenoy V B, Saam W F *Phys. Rev. Lett.* **75** 4086 (1995)
131. Dietrich S, Napiorkowski M *Phys. Rev. A* **43** 1861 (1991)
132. Indekeu J O, van Leeuwen J M J *Physica C* **251** 290 (1995); *Physica A* **236** 114 (1997)
133. Boulter C J, Clarysse F *Phys. Rev. E* **60** R2472 (1999)
134. Ross D, Bonn D, Meunier J *Nature* **400** 737 (1999)
135. Pfohl T, Riegler H *Phys. Rev. Lett.* **82** 783 (1999)
136. Bertrand E et al. *Phys. Rev. Lett.* **85** 1282 (2000)
137. Ross D, Bonn D, Meunier J *J. Chem. Phys.* **114** 2784 (2001)
138. Rafaï S et al. *Phys. Rev. Lett.* **92** 245701 (2004)
139. Rafaï S, Bonn D, Meunier J *Physica A* **358** 97 (2005)
140. Swain P S, Parry A O *Europhys. Lett.* **37** 207 (1997)
141. Parry A O, Swain P S *Physica A* **250** 167 (1998)
142. Indekeu J O et al. *J. Stat. Phys.* **95** 1009 (1999)
143. Clarysse F, Boulter C J *Physica A* **278** 356 (2000)
144. Sartori A, Parry A O *J. Phys. Condens. Matter.* **14** L679 (2002)
145. Fenzl W *Europhys. Lett.* **64** 64 (2003)
146. Yochelis A, Pismen L M *Colloids Surf. A* **274** 170 (2006)
147. Ragil K et al. *Phys. Rev. Lett.* **77** 1532 (1996)
148. Shahidzadeh N et al. *Phys. Rev. Lett.* **80** 3992 (1998)
149. Straumal B B, Kogtenkova O, Zieba P *Acta Mater.* **56** 925 (2008)
150. Straumal B B et al. *Phil. Mag. Lett.* **87** 423 (2007)
151. Straumal B et al. *Mater. Sci. Eng. A* **495** 126 (2008)
152. Massalski T B et al. (Eds) *Binary Alloy Phase Diagrams* (Materials Park, OH: ASM Intern., 1993)
153. Straumal B et al. *Acta Mater.* **56** 6123 (2008)
154. Hasson G C, Goux C *Scripta Metall.* **5** 889 (1971)
155. Divinski S V et al. *Phys. Rev. B* **71** 104104 (2005)
156. Pandit R, Schick M, Wortis M *Phys. Rev. B* **26** 5112 (1982)
157. Chang L-S et al. *J. Phase Equil.* **18** 128 (1997)
158. Chang L-S et al. *Scripta Mater.* **37** 729 (1997)
159. Chang L-S et al. *Defect Diff. Forum* **156** 135 (1998)
160. Chang L-S et al. *Acta Mater.* **47** 4041 (1999)
161. Straumal B, Sluchanko N E, Gust W *Defect Diffusion Forum* **188–190** 185 (2001)
162. Straumal B et al. *Defect Diffusion Forum* **194–199** 1343 (2001)
163. Chang L-S et al. *Acta Mater.* **55** 335 (2007)
164. Straumal B B et al. *Acta Mater.* **53** 247 (2005)
165. Bian B et al. *Acta Mater.* **245** 118632 (2022)
166. Prokoshkina D et al. *Acta Mater.* **61** 5188 (2013)
167. Divinski S V, Reglitz G, Wilde G *Acta Mater.* **58** 386 (2010)
168. Zhang L et al. *Comput. Mater.* **7** 1 (2021)
169. Hellman O C et al. *Microsc. Microanal.* **6** 437 (2000)
170. Luo J et al. *Science* **333** 1730 (2011)
171. Gupta V K et al. *Acta Mater.* **55** 3131 (2007)
172. Korolev V et al. *Scr. Mater.* **186** 14 (2020)
173. Yu Z et al. *Science* **358** 97 (2017)
174. Zhou N et al. *Scr. Mater.* **130** 165 (2017)